ECO2 project number: 265847

Deliverable Number D3.3: Technical modeling report
WP3; lead beneficiary number 21 (HWU)

Technical report on verified and validated application of droplet/ bubble plume-, geochemical- and general flow- models.

Authors:

Marius Dewar[1], Baixin Chen[1], Yakushev Evgeniy[2], Helge Avlesen[3], Guttorm Alendal[4], Alfatih Ali[4], Lisa Vielstädte[5]

[1]Institute of Mechanical, Process and Energy Engineering, Heriot-Watt University Edinburgh, UK

[2]NIVA, Norwegian Institute for Water Research, Oslo, Norway

[3]Uni Computing, Bergen, Norway

[4]Department of Mathematics, University of Bergen, Bergen, Norway

[5]Helmholtz Zentrum für Ozeanforschung Kiel GEOMAR Kiel, Germany.

Contents

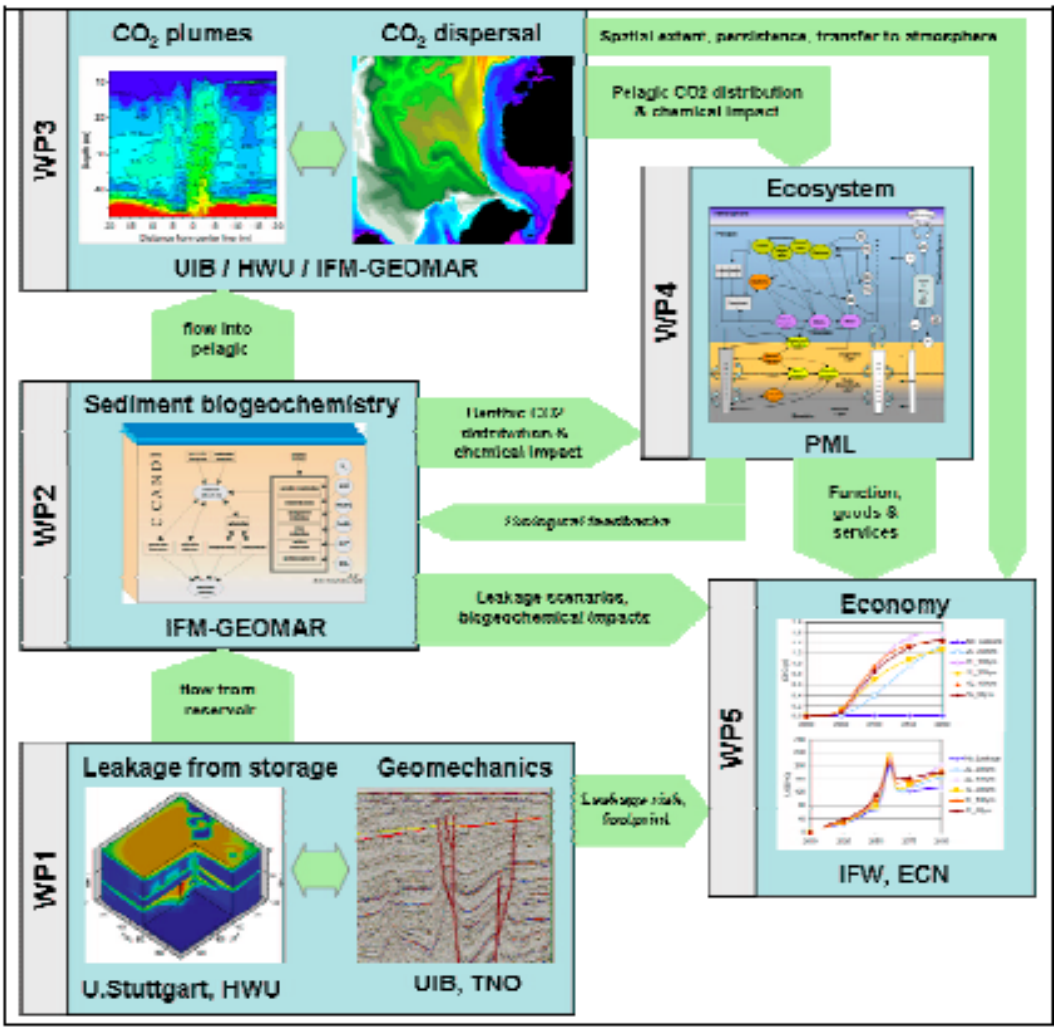

Fig. 0-1, The schematic description of the models developed from each WP and the details of WP3 models are introduced and discussed in this report.

Within WP3 there are three classes of models; A marine chemistry model, two different Near-field two-phase plume models, NFTPM, and a regional scale general circulation model (BOM, Bergen Ocean Model). They all have different needs with regards to data for calibration and validation. This report will document the effort made so far to prepare the suit of models to perform the scenarios.

Due to the extensive ECO2 cruise program, new and pristine data sets have become available. The use of these data sets to develop and validate the different models is still on going; hence further enhancement in predictability and reliability is to be expected as the different data sets are synthesised. Including field observation of bubble plume, oceanography, turbulent current, metocean, and the biochemistry. See also ECO2 D3.1 for a general discussion on model parameters.

The spatial (temporal) scales of the model framework used within WP3 cover the spatial (temporal) ranges from 10^{-2} m (minutes) of biogeochemical transfer and leaked bubble dynamics; through 10^{3} m (hours to days) of the near-field plume and acute impacts (Near-field two-phase plume model, NFTPM); to $10^{6} \sim 10^{7}$ m (weeks to months) of leaked CO_2 dispersion and transport in North Sea (Bergen Ocean Model (BOM)). This is a challenge, especially when coupling the different models together.

Off-line transfer of data between different models has been tested in term of one-way uploading; e.g., the output of acute pCO_2 changes simulated by near-field two-phase plume model (NFTPM) has been used as source terms in the BOM set up of the North Sea. Furthermore, tests of two-way off-line nesting, such as forcing the NFTPM with statistical current data generated by BOM, or nesting the biogeochemical transportation model to a plume model are underway. .

INTRODUCTION

Modelling the fate of CO_2 seeped through the seafloor will be important in many aspects during planning, operational, and closure phases of a sub-sea geological storage project. How the leaked CO_2 is transported and diluted in the water masses will influence on the magnitude of the spatial and temporal environmental footprint a leak might impose. Increased CO_2 concentration leads to acidification of the water masses that might cause impact on the marine ecosystem (Blackford et al, 2010). How far away from a leak it is detectable will influence on the design of a monitoring program. Further, how the CO_2 is transported by local currents will determine whether it might reach the surface, with subsequent outgassing to the atmosphere.

CO_2 might reach the marine environment along many pathways. Part of leaked CO_2 might be dissolved in seafloor sediments, creating negative buoyant water parcels that will tend to migrate in the horizontal and might accumulate in topographic depressions. However, boundary layer turbulence might still bring CO_2 into the water column (Rygg, et al. 2011). Pure CO_2 will be less dense than seawater at depth shallower than approx. 3500 meters, and will be in gaseous phase if shallower than 500 meters depth. Hence the most likely scenario is that a leak will create droplets (liquid) or bubble (gaseous) ascending through the water column. Since the site of study will be the Sleipner area of around 90 meters depth the focus here will be on bubbles.

As the bubbles (the dispersed phase, with size up to 20 – 30 mm) ascend the surrounding water masses (the carrier phase) there will be a two way dynamical coupling. The magnitude of influence from the dispersed phase will depend on bubbles sizes and amount of bubbles being present. The most dominant processes will be interfacial drag from individual bubbles, retarding the bubble ascent and creating a lifting force to the carrier phase. This entrained water will be lifted upward into, in case of stratification, a less dense environment. Simultaneously the CO_2 gas within the bubble will be transferred through the interface and dissolved into the surrounding water, increasing the density. Hence, the

entrained water will be negatively buoyant. The combination of these processes, coupled with a dynamically active water column, creates bubbles plumes. Simulating such events is challenging, especially due to the many different scales that are involved.
The development and verification of a near-field, at scales from 10^{-2} m of bubbles to 10^{3} m of the CO_2 enriched seawater plume, multiphase plume model are the integration of sub-models for plume dynamics through exchanges in momentum and mass between dispersion phase and the ambient environment (currents, temp/salinity profiles).

Useful data includes the physicochemical properties and turbulent velocity profiles in the ocean at specified depths and locations and the data of CO_2 droplet/bubble dynamics including the rising velocity and shrinking rate. Such set of data can be used for the model calibration and validation.

While waiting for release of data from the ECO_2 field campaign; the models have been calibrated and validated through for data currently available in literature. As new data is released from ECO_2 cruises they will be utilized to further improve the models.

The local current and stratification will influence on the evolvement of the plume, variability in current direction and speed will make the spatial footprint highly time dependent. These local currents will also transport the dissolved CO_2 as a passive tracer once it has been diluted enough to make it a passive tracer. To prepare for the Sleipner scenarios the Bergen Ocean Model (BOM) has been set up for the North Sea. Tidal forcing and wind taken from spring 2012 have been used to drive the model. This period has been chosen due to the number of ECO2 cruises to the Sleipner area in that period.

While waiting for the data from these cruises to be released BOM has been validated by assuring that the modelled currents capture well known features of the circulation in the North Sea. Three alternative methods for including leakage of CO_2 into the water column have been implemented, and preliminary results are being shown.

A simple standard for data flow between models of the different work packages has been agreed upon; one should use the NetCDF binary file format that should too as large a degree as possible follow the Climate and Forecast metadata convention from http://cf-pcmdi.llnl.gov/.

As part of the development of a simulation framework necessary for risk/impact assessment research has been carried out on the modeling of biogeochemical transactions between sediment and bottom water. A one-dimensional C-N-P-Si-O-S-Mn-Fe vertical transport-reaction model is developed for describing both the sediment and bottom boundary layers coupled with biogeochemical block simulating changeable redox conditions, and the carbonate system processes block. The main focus of this investigation relates to the Bottom Boundary Layer, the most active zone of interactions. Organic matter formation and decay, reduction and oxidation of species of nitrogen, sulfur, manganese, iron, and the transformation of phosphorus species are parameterized in the model. The model will use for validation the data from the field studies and laboratory experiments (in particular the sediment-water fluxes measurements).

PART I: MODELLING OF THE NEAR FIELD IMPACT OF LEAKED CO_2

INTRODUCTION

Near-field multiphase model (NFMPM) is the model to predict the acute impact of leaked CO_2 on the marine environment. The space scale is ranging from centimetres to several kilometres and time scale from seconds to days. The data of porosity of the sediments, the topography of seafloor, the vertical (and horizontal if available) distribution of local current, temperature, salinity and background pCO_2, are requested for reconstruction of a near-field scale turbulent ocean. Those data can be the field observation data or the data predicted from up-scale model (regional OGCM). The CO_2 leakage flux and sites (area) are the data for generation of plume of dispersed phase.

The outputs from this NFMPM, such as the pH/pCO_2 changes, can be applied for prediction of acute biological impacts and as the input data to the up-scale model (regional scale OGCM) for long-term impact predictions. For the case of 'CO_2 eruption', which may occur if stored CO_2 leaks from the geological failures, the NFMPM serves as prediction of the evolution of CO_2 volcanoes and the acute local marine physicochemical impacts.

The model is introduced in the way of what leakage may occur, and begins with the leaked bubble formation from sediments, the fate of individual bubble in the ocean, and then the two plumes interaction and development.

MODELLING OF FATE OF INDIVIDUAL CO_2 BUBBLE IN SEAWATER

A set of models has been developed and calibrated with available data for prediction of the dynamics of an individual CO_2 bubble/drop leaked from seabed. This includes the models estimating the initial size of the CO_2 bubble/drop formed through the sediments and predicting the ascent rate and shrink rates of a free rising CO_2 bubble/drop. Models are calibrated with the data collected in terms of effective drag coefficient (C_d) for ascent rate, Sherwood number (Sh) for effective mass transfer, and then the fate of individual bubble

in ocean. The correlations of Cd and Sh are selected and proposed to the application to ECO2 project.

Modelling of initial bubble size formed on sediments

Leaked CO_2 into water column is in the form of gas bubble or droplet depending on the depth of the leakage sites. The initial bubble and droplet size (or equivalence diameter) is vital as it determines the rate at which the CO_2 rises and the rate of dissolution. Leakages of larger bubbles or droplets have more buoyancy and therefore rise faster, whereas smaller bubbles and droplets have more interfacial area at given leakage rate, so will dissolve quicker.

Flows through the sediments are slow maintaining a continuous fluid through imbibition and drainage flows (Silin et al., 2009), reaching the surface the plume becomes free rising in the waters with a breakup of the fluid into droplets or bubbles due to Rayleigh instabilities. The diameter (d_{eq} m) of the forming bubbles or droplets can be predicted through a simple force balance, where the CO_2 will remain attached to the sediment until buoyancy (first term at left hand side of Eq. 1) and drag forces (second term at left hand side of Eq.1-1) exceed the tension between the bubble/droplet and the sediment surface (right hand side of Eq. 1-1) (Kulkarni and Joshi, 2005). This formation is controlled through the pore channel area unless there are very high flow rates affecting bubble sizes (Wüest et al., 1992).

With an individual bubble or droplet forming from a sediment channel under seawater, its shape considered a sphere and tension applied from the circumference of the sediment channel, the force balance is defined by the sum of the force vectors through the relation:

$$\left[\left(\rho_w-\rho_C\right)g\frac{d_{eq}^3}{6}\right]^2+\left[\frac{C_d}{8}\rho_w u_{rd}^2 d_{eq}^2\right]^2=\left[d_{ch}\left(\sigma_{C,sed}+\sigma_{w,C}\right)\right]^2 \qquad (1\text{-}1)$$

As this relation assumes that there is a low flow rate, the pressure effects are neglected. At larger flow rates, the bubbles or droplets would be forced out of the channel by pressure increasing the possibility of merging of bubbles or droplets. Collisions of bubbles or droplets from multiple channels are also neglected within this study.

A range of diameters is therefore produced depending on the ocean currents, leakage depths and channel diameters. It is very difficult to estimate the size of the sediment channels, which strongly depends on the geological properties and the structures of sediments, and should be decided by in situ observation data.

Here a very preliminary approach is tested by using the sediment porosity based on the assumptions that the number of sediment channels is equal to the number of sediment particles and that the sediment particles are the spherical, the channel diameter can be approximately estimated,

$$d_{ch} = d_{sed}\sqrt{\frac{\phi}{(1-\phi)}} \qquad (1\text{-}2)$$

Surface and interfacial tension between CO_2, water and solid substrate have been applied from Espinoza and Santamarina (2010) based on pressures at depth. Data for the porosity (Φ=0.35) and the diameter of the larger sediments particles (d_{sed}= 1 – 8mm) are provided by data from samples taken from the west coast of Scotland (QICS, 2012). This is not to be taken as an established calculation for channel diameter due to the high percentage of finer sand particles within the surface sediments (McGinnis et al., 2011). Further assumptions include a constant value over time, therefore sediment particles taken up through the eruption at high leakage rates, and falling debris at low leakage rates (Esposito et al., 2006) are neglected.

Model test and calibration

The variations in sediments across the North Sea and the west coast of Scotland will have an impact on how the bubbles and droplets form. For these reasons, Eq. (1-1) will therefore be taken only as a predictive indication of the bubble size that can be formed.

A range of bubble and droplet diameters are calculated dependent on the leakage depth and how water currents and leakage channels vary across the simulation. The effect of varying the depth, sediment particle size and seawater currents on the initial droplet or bubble diameter can be seen in Fig. 1-1. For constant water currents and temperatures (Fig. 1-1a); as the pressure increases, the bubble diameters decrease. This means that the reduction in

tension has a more pronounced effect than the decrease in buoyancy force with depth. For droplets, the surface tension levels out as the phase changes, however a large decrease in buoyancy force allows the droplets to greatly increase in diameter before breaking off the sediments. Increased currents create an increase in hydrodynamic force acting against the surface tension, producing smaller bubbles or droplets, as predicted for bubble data sets at depth of 100 m in Fig. 1-1b. A good match can also be seen between the experimental range for CO_2 droplet formation provided by Nishio et al. (2005) and those calculated by Eq. (1-1) using pressure, temperature, density and channel diameter data from the experiment.

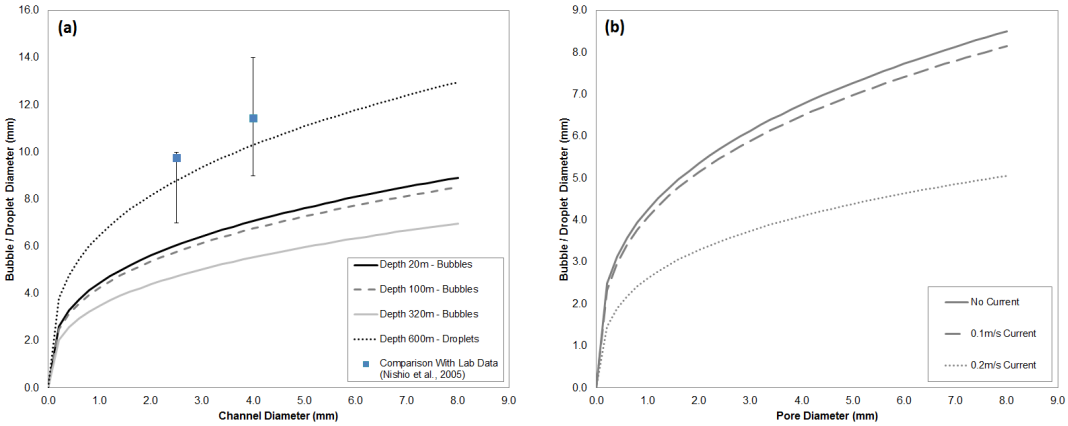

Fig. 1-1. The size of the initial bubble and droplet formations. (a) At varied depths with no seawater currents, including those for droplets (squares) falling within the experimental range error bars from Nishio et al. (2005); (b) 100 meters depth with varied water currents.

Modelling of CO_2 bubble free rising in seawater

Inter fluid momentum exchange is caused through buoyancy within the dispersed CO_2 plume, and transferred to the carrier plume through drag force. Correlations for the drag coefficient of bubbles and droplets are available; many of these cover bubbles or droplets individually (Chen et al., 2003; 2005; 2009; Gabitto and Tsouris, 2005; McGinnis et al., 2006; Mori and Mochizuki, 1998; Ozaki et al., 2001; Sato and Sato, 2002). Others reduce the correlation to cover a range of bubbles and droplets, taking hydrates and the shape deformation into account through use of the Eötvös and Morton numbers (Kano et al., 2009; 2010; Gangstø et al., 2005; Bozzano and Dent, 2001; Bigalke et al. 2008; 2010).

It was found that there was not one individual model that has a good fit for the experimental data covering each phase. Four different trends can be seen in the experimental data linked to each phase shown by the data in Figure 1-2; therefore, a best fit model is proposed using a friction factor, $f(\mathrm{Re})$, to cover the phase and presence of hydrates based on the experimental data from Bigalke et al. (2008; 2010), Ozaki et al. (2001), Clift et al. (1978), Haberman, and Morton, (1954), Johnson, et al (1969), Baird and Davidson (1962), Davenport et al. (1967) and Guthrie and Bradshaw (1967).

$$C_d = \frac{24}{\mathrm{Re}} f(\mathrm{Re}) \qquad (1\text{-}3)$$

Correlations for the friction factor as a function of Reynolds number are developed through curve fitting for CO_2 droplets and bubbles, formulated using constants data given in Table 1-1:

$$f(\mathrm{Re}) = 1 + 0.045\,\mathrm{Re} - A\,\mathrm{Re}^2 + B\,\mathrm{Re}^3$$

Table. 1-1. A and B constants for drag friction factor

	A	B
Droplet without Hydrate:	1.50×10^{-4}	1.60×10^{-7}
Droplet with Hydrate:	7.50×10^{-5}	8.00×10^{-8}
Bubble without Hydrate:	1.50×10^{-4}	3.20×10^{-7}
Bubble with Hydrate:	1.20×10^{-4}	3.20×10^{-7}

This correlation is valid for bubbles at Reynolds numbers up to 400 and droplets at Reynolds numbers up to 800 (1200 with hydrate). Beyond this, the model from Bozzano and Dent (2001) is employed:

$$C_d = f\left(\frac{a}{R_0}\right)^2 \qquad (1\text{-}4)$$

where the friction factor f is found to be:

$$f = \frac{48}{\mathrm{Re}}\left(\frac{1+12M^{1/3}}{1+36M^{1/3}}\right)+0.9\frac{Eo^{3/2}}{1.4\left(1+30M^{1/6}+Eo^{3/2}\right)}$$

and the deformation factor $(a/R_0)^2$ is found to be:

$$\left(\frac{a}{R_0}\right)^2 = \frac{10\left(1+1.3M^{1/6}\right)+3.1Eo}{10\left(1+1.3M^{1/6}\right)}$$

Model calibration

Data for the rising velocity of various gasses has been collected from Bigalke et al. (2008; 2010), Ozaki et al. (2001), Clift et al. (1978), Haberman, and Morton, (1954), Johnson, et al (1969), Baird and Davidson (1962), Davenport et al. (1967) and Guthrie and Bradshaw (1967). Data has also been collected from the QICS project (2012) to be included in due course. From the rising velocity, particle size and fluid properties, a correlation can be developed for the drag coefficient (C_d) against Reynolds number (Re) based on this data. The correlation of C_d for CO_2 bubble was modified to fit the data based on the version developed during the first year study. A best fit model is proposed using a friction factor, *f*(Re), to cover the phase and presence of hydrates and can been seen matching the available data in Fig.1-2.

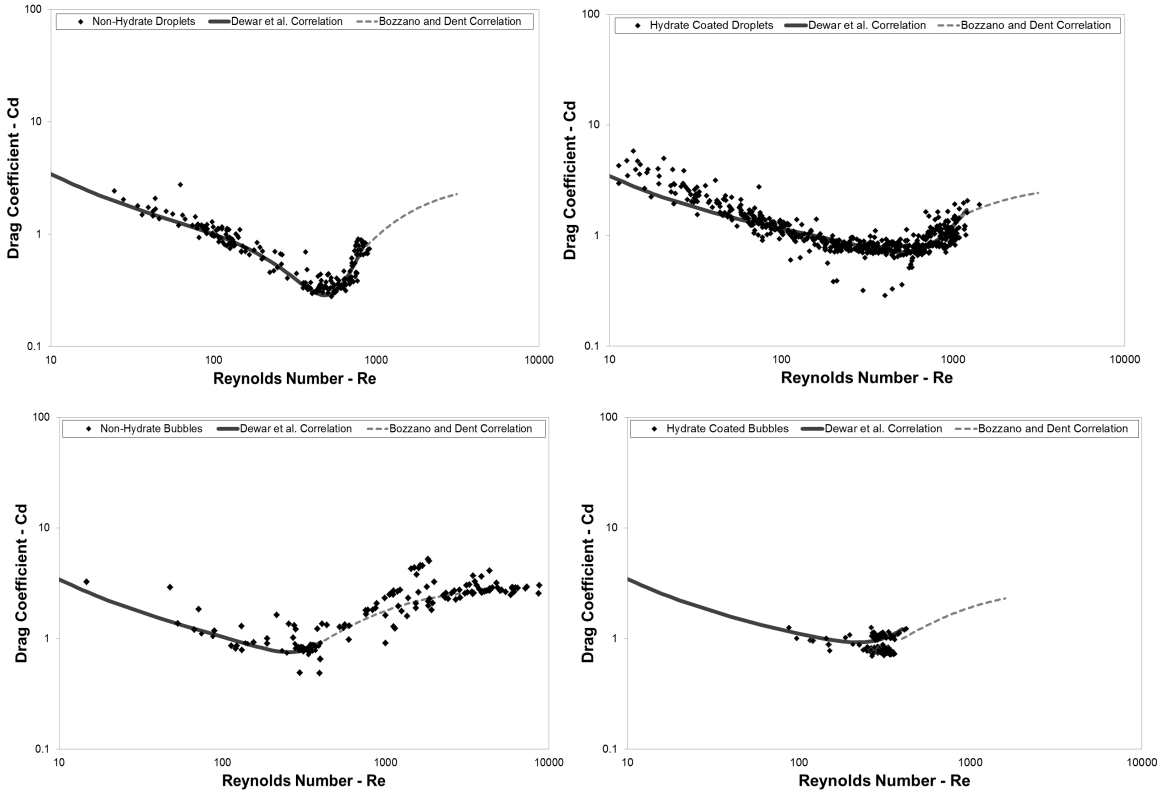

Fig.1-2. Experimental data for drag coefficient A) droplets, B) droplets with hydrates, C) bubbles, D) bubbles with hydrates, showing the differences in the phase and presence of hydrates.

The properties calculated above do not take into account any helical or horizontal movements whilst the bubble or drop is rising as they are assumed to be traveling linear vertically. Horizontal movement would reduce the total rise distance and perceived velocity. As show in Fig.1-2 (Dewar et al., 2013), formation of the hydrate film on the interface between the particle and water makes a difference in the rising dynamics of the bubble/droplet. This effect should be predicted by developing the individual models.

Modelling of rising CO_2 bubble dissolution in seawater

Zheng and Yapa (2002) proposed correlation of the Sherwood number for bubbles based on equations developed by Clift et al. (1978) and Johnston et al. (1969). The effective shrinking rate can be estimated by:

$$Sh = f_k(d_{eq}, u_{rd}) \cdot \frac{d_{eq}}{D_f^{1-n}} \qquad (1\text{-}5)$$

with an index of n = 0.5 for the diffusivity, d_{eq} as the equivalent diameter and u_{rd} as the relative droplet velocity; the function f_k varies dependent on the bubble diameter:

$$f_k(d_{eq}, u_d) = \begin{cases} 11.3\left(\frac{u_{rd}}{0.45 + 20 d_{eq}}\right)^{0.5} & d_{eq} < 5mm \\ 6.5 & 5mm < d_{eq} < 13mm \\ \frac{0.219462}{d_{eq}^{0.25}} & d_{eq} > 13mm \end{cases} \qquad (1\text{-}5b)$$

Model testing and calibration

As of yet there is not enough on-site experimental data for CO_2 bubbles or droplets to verify the model dynamics and dissolution of the CO_2. It is difficult to perform lab or in-situ experiments due to the velocity of the bubbles and droplets which requests a large vertical channel lab facility, or fast moving AUV which will manipulate results due to induced momentum. A suggestion has been proposed for further on site experiments in which 2 points measure the bubble size and from this calculate the average dissolution rate.

The Lab experiment data from 3 sets of CO_2 bubble without hydrate dissoltion in water and one set of O_2 dissolution in water (Fig. 1-3) shows a good correlation between Sherwood number (Sh) and the bubble size.

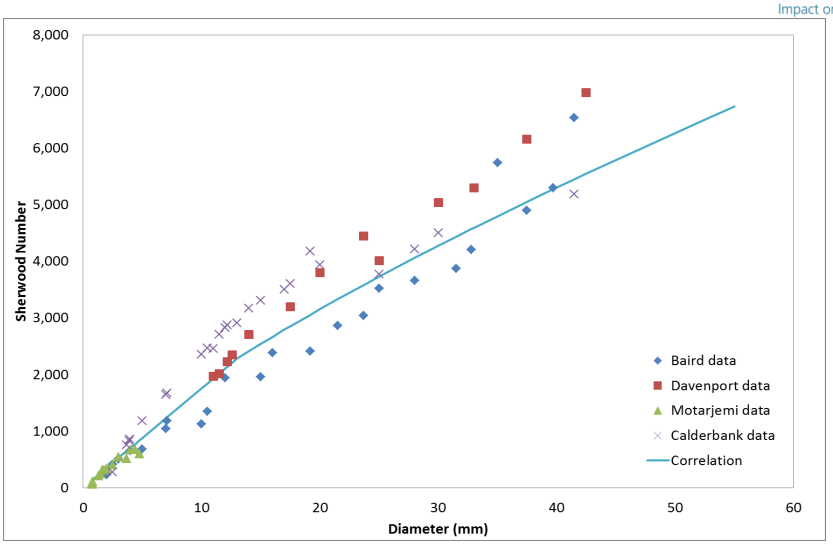

Fig.1-3 Showing the Sherwood number experimental data, for CO_2 experiments in tap water, blue diamonds from Baird and Davidson (1967) and red squares from Davenport et al. (1962). CO_2 experiments in aqueous glycerol solution, purple crosses from Calderbank et al., (1970). For O_2 experiments, green triangles from Motarjemi and Jameson (1978). Listed by Zheng and Yapa, (2002).

Model of the fate of a free rising bubble in ocean

The dynamics of free-rising CO_2 bubbles leaked from seabed, including dissolution and buoyant ascending, can be simulated by the dynamics of an individual bubble when a further assumption made that the collision and collection among bubbles could occur negligibly. The mass and momentum conservative equations of an individual bubble are:

$$\frac{du_r}{dt} = \frac{\rho_s}{\rho_c}((1.0 - \frac{\rho_c}{\rho_s})g - \frac{3u_r^{\,2}}{4D}C_d) - u_r\frac{d\ln(m_c)}{dt} \qquad (1\text{-}6)$$

$$\frac{dd_e}{dt} = -\frac{1}{\rho_c}(\frac{d_e}{3}\frac{d\rho_c}{dt} + 2k(C_s - C_0)) \qquad (1\text{-}7)$$

where u_c is bubble velocity relative to seawater (m/sec), m represents mass of bubble (kg), C is the CO_2 concentration (kg m^{-3}). The subscripts of 'c', 'cs' and 's' indicate CO_2, CO_2 bubble surface, and seawater, respectively.

In Eq. (1-6), the first term is the contribution due to the CO_2 expansion (positive) or compression (negative), while the second is the dissolution, which is always negative with

the bubble shrinking. The first term in Eq. (1-7) is the buoyancy term that acts against the drag, the second term. The last term is the additional mass force due to the mass change through dissolution. The governing equations of an individual bubble/drop free rising in seawater are solved numerically along with the sub-models proposed in the previous sections, such as the sub-model of the physical properties of a CO_2/seawater system, the effective drag coefficient, and effective mass transfer coefficient.

To validate the model, CH_4 bubble data has been taken from an experimental release within Monterey Bay by Rehder et al. (2002). Taking CH_4 bubble solubility from Duan et al. (2006) and from Tishchenko et al. (2005) with hydrate along with the hydrate stability prediction and the diffusivity of CH_4 has been taken from Jähne et al. (1987). The density of the CH_4 is taken from the National Institute of Standards and Technology (NIST), and the dissolved CH_4 solution is derived from Duan et al. (2006).

It can be seen from the comparison between the simulation results and the data that the proposed submodels (Cd and Sh) provides a good agreement between available experimental data and our simulations. See Fig.1-4 and Fig.1-54.

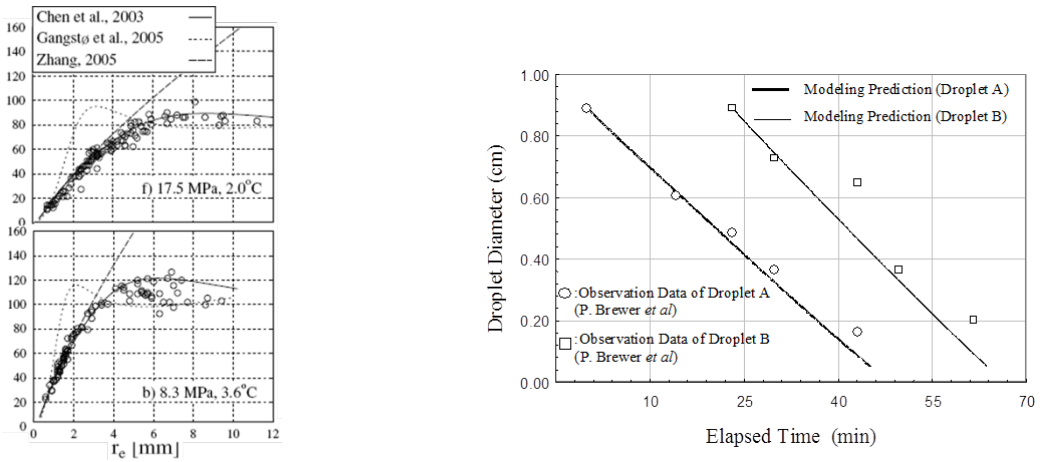

Fig.1-4a) individual droplet model against lab experimental data for carbon dioxide droplets by Bigalke et al. (2008, 2010); Fig.1-4b) model against in-situ experimental data for carbon dioxide droplets by Brewer et al. (2006).

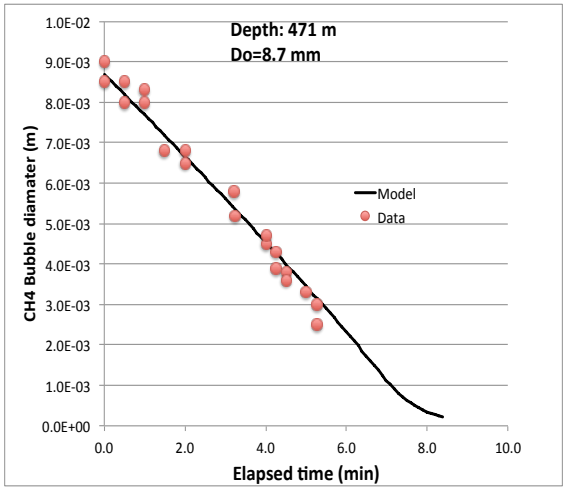

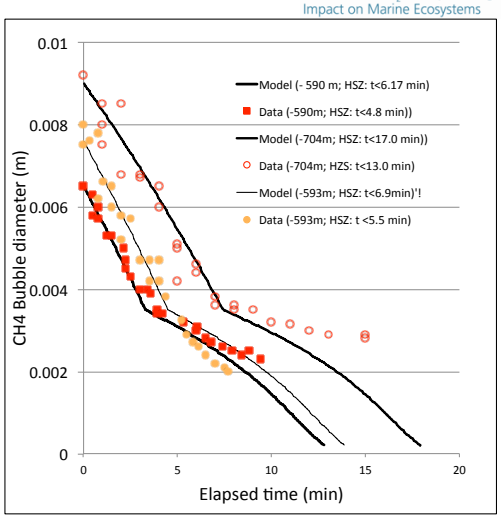

Fig.1-5a) individual bubble model against experimental data for methane bubbles by Rehder et al. (2002); Fig.1-5b) model against experimental data for methane bubbles in the hydrate stability field by Rehder et al. (2002).

From the above, it can be seen that the model works well for the different gasses and liquid droplets within the waters. Therefore two-phase plume simulations of leakage are simulated from within the North Sea, to compare how the gas dynamics vary.

Bubble dynamic models developed by Geomar (Geomar model)

Bubbles leaked from seabed and ascending the water-column, can be simulated by the dynamics of individual bubbles, assuming that bubbles of the same initial size behave identical and bubble collision and breakup are negligible. Mass-balance equations are solved simultaneously for implemented gas species (i.e. CO_2, CH_4, O_2, N_2, Kr, and H_2S), simulating gas stripping from ambient seawater (i.e. O_2 and N_2) as well as the dissolution of bubbles with a mixed gas composition.

The rate of gas transfer at the bubble-water interface:

$$\frac{\partial N}{\partial t} = -NF * A_B * K_L * \Delta C \qquad (1\text{-}8)$$

where NF is the number flux of bubbles per time, A_B is the bubble surface area, K_L is the gas specific mass transfer velocity, and ΔC is the gas concentration gradient at the bubble-water interface (McGinnis and Little, 2002). The model is based on the discrete bubble

dissolution model of McGinnis and Little (2002) but has a modified parameterization regarding the solubility of CO_2 using the Equation of State (EOS) given by Duan et al. (2006). The EOS explicitly accounts for pressure-effects that become important already at water depths larger than 50 m and consequently need to be considered for Sleipner scenarios (~80 m water depth).

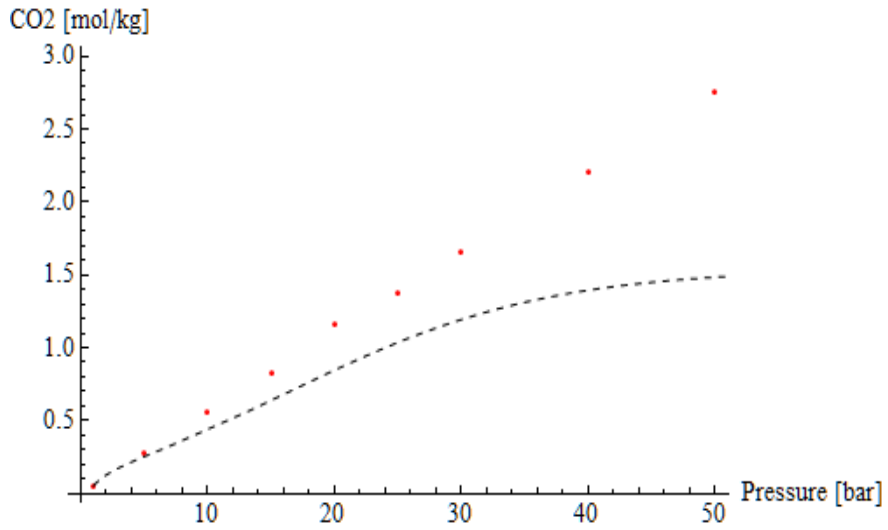

Fig.1-6 Showing the modelled solubility of CO_2 as a function of pressure (at 8°C and 35 PSU) calculated by application of Henry's Law (red dots) and the EOS given by Duan et al.,2006 (dashed line).

Sets of empirical mass transfer correlations, both for clean and dirty bubbles, have been suggested (McGinnis et al., 2006; Leifer et al., 2002; Zheng and Yapa, 2002). Zheng and Yapa (2002) proposed the following empirical equations, as a combination of the equations originally developed by Johnson et al. (1969) and Clift et al. (1978),

(i) For bubbles with spherical shape (*small size range with r <2.5 mm*):

$$K_L = 0.0113 \times \left(\frac{vb \times Di}{0.45 + 0.4r}\right)^n$$

(ii) For bubbles with ellipsoidal shapes ($2.5 \leq r \leq .6.5\ mm$)

$$K_L = 0.065 \times Di^n$$

(iii) For bubbles with spherical-cap shape *(large size range with r> 6.5mm*)

$$K_L = 0.0694 * 2r^{-0.25} \times Di^n$$

Above equations give the mass transfer coefficient [m/s] for various bubble shapes and sizes, where the bubble radius, *r,* is given in [cm], and the molecular diffusion coefficient of the considered gas in water, *Di*, is given in [cm/s^2]. The exponent, *n*, has been determined as 0.5 and 0.67 to calculate mass transfer velocities for clean and dirty bubbles, respectively. Zheng and Yapa (2002) tested this set of equations for CO_2 bubbles in fresh water and in 96% aqueous solution, respectively under atmospheric pressure and room temperature. Even though the model predicts experimental data very well, it should be noted that the pressure effects at greater water depths have not been studied experimentally and are not fully understood from a theoretical perspective (Chen et al., 2009). Geomar currently evaluates shallow optical and geochemical field data (Panarea 2013) to test the empirical equations of CO_2 mass transfer. However, according the necessity of high-pressure data (~1MPa) further research is planned for the upcoming Panarea cruise in 2014.

An empirical correlation, based on experimental data, was presented by [*Wüest et al.,* 1992]

$$U_T = \begin{cases} 4474r^{1.357} & r < 0.69mm \\ 0.23 & 0.69mm < r < 4.9mm \\ 4.202r^{0.547} & r \geq 4.6mm \end{cases} \qquad (1\text{-}10)$$

and is being used in the *Geomar model.* This model shows consistency with observations of the Geomar gas release experiment, where single gas bubbles rose in the absence of bubble plume dynamics. However, natural gas bubbles (Panarea) exceeded modelled rise velocities, which were significantly faster. Optical data are currently evaluated and correlated to seepage activity (gas flux) to develop additional parameterization of entrained water velocity as a critical gas flux is exceeded.

LAB. and Field Experiment Data

The improvement and validation of numerical models is reliant on qualitative data sets obtained either from natural analogues or experiments. Within the scope of the ECO2 project, data has been collected during field campaigns to a natural seepage site offshore Panarea (ECO2-3**,** ECO2-8) and to the Sleipner area in the North Sea (CE12010). Data includes physicochemical properties, geochemical- and current flow measurements. Partly, optical data of bubbles and bubble plume dynamics are available (i.e. rise velocity, size distribution, and bubble shrinkage).

Particularly, the experimental release in the Sleipner area offered unique data to study potential CO_2 leakage in the North Sea. Despite the low leakage rate (~130 kg/day) and temporal limitation (~15 h) the effects of leakage could be measured under North Sea tidal forcing and physicochemical conditions. The experiment and modelling indicate that the impact of leakage at a rate comparable to the experiment is limited to bottom waters (1-5 m above ground depending on the initial bubble size) and a small area around the gas source (50 m). North Sea tidal cycles make the spatial footprint of a leak highly time dependent and strong currents significantly diminish the risk for the far-field of a leak, by efficiently diluting the solute in ambient seawater.

Optical measurements of bubble plume dynamics (i.e. bubble rise velocity, shrinkage rate, entrainment, and detrainment) can be used to validate the bubble dissolution model. Obtained data indicate the occurrence of additional momentum (entrained water) as a critical gas flux is exceeded (ECO 2-8), which needs to be implemented to the model. Current parameterization is only consistent with velocity data of discrete bubbles that rose in the absence of plume dynamics.

The initial bubble size spectrum is crucial as it determines the rate at which the CO_2 rises and the rate of dissolution into the water-column. Image and video data are available for CO_2 bubbles seeping at Panarea and CH_4 bubbles leaking at abandoned wells in the North Sea (Sleipner area). Latter could be particularly used as input parameter for CO_2 leakage simulations in the North Sea as leakage depth, hydro-physical conditions, and sediment characteristics are supposed to be comparable.

As a leak has been detected and located at the seafloor, the question raised is how much carbon dioxide is leaking into the water-column. The temporal variation of stationary pCO_2 measurements correlated to local current data will provide information on leakage activity. Obtained gas flux measurements enable to test the applicability of the plume dispersion model to quantify CO_2 leakage rates based on geochemical and hydro-physical measurements (ECO2-8). The development of such a monitoring tool would be highly beneficial to quantify CO_2 fluxes into the water-column over short to longer time-periods. Because data has not yet been published in literature any details have been excluded from this public report.

Modelling of near-field physical-chemical impacts of leaked CO_2 on ocean

Governing equations for CO_2 and seawater plumes

The CO_2 bubble plume is referred to as the dispersed phase (subscript *d*), and the seawater carrier phase (subscript *c*), with the void fraction α calculated as:

$$\alpha_c + \alpha_d = 1$$

The large eddy simulation based governing equations for the seawater carrier phase are defined as:

$$\frac{\partial \bar{\rho}}{\partial t} + \frac{\partial \bar{\rho} u_i}{\partial x_i} = \dot{w}_{co_2} \tag{1-11}$$

$$\frac{\partial \bar{\rho} u_i}{\partial t} + \frac{\partial \bar{\rho} u_i u_j}{x_j} = -\frac{\partial \hat{p}}{\partial y} + \frac{\partial D_{ij}}{\partial x_i} + (\bar{\rho} - \rho_0) g + \dot{F} \tag{1-12}$$

$$\frac{\partial \bar{\rho} \hat{\phi}_k}{\partial t} + \frac{\partial \bar{\rho} \hat{\phi}_k u_j}{\partial x_j} = \frac{\partial}{\partial x_j}(\bar{\rho} D_k \frac{\partial \hat{\phi}_k}{\partial x_j}) + \frac{\partial \bar{\rho} \hat{q}_k}{\partial x_j} + \dot{w}_{co_2} \tag{1-13}$$

and the governing equations for the dispersed bubbles phase as:

$$\frac{\partial \hat{n}_d}{\partial t} + \frac{\partial \hat{n}_d u_{di}}{\partial x_i} = \hat{q}_{dn} \quad (1\text{-}14)$$

$$\frac{\partial \hat{\alpha}}{\partial t} + \frac{\partial \hat{\alpha} u_{dj}}{\partial x_j} = \hat{q}_{dco_2} - \frac{\dot{w}_{co_2}}{\rho_d} \quad (1\text{-}15)$$

$$\frac{\partial \overline{\rho}_d u_{dj}}{\partial t} + \frac{\partial \overline{\rho}_d u_{di} u_{dj}}{\partial x_j} = \hat{\alpha}(\overline{\rho}_d - \rho_w)g - \dot{F} \quad (1\text{-}16)$$

where $\overline{\rho}$ is the bulk density, (kg/m^3), u is the velocity (m/s), t is the time (s), x is the distance (m), $\dot{w}$ is the mass exchange rate (kg/m^3·s), p as the hydrostatic pressure (Pa), D is the dissipation term (kg/m·s^2), ρ_0 in the initial density (kg/m^3), g is gravity (m/s^2), $\dot{F}$ is the momentum exchange rate (kg/m^2·s^2), $\hat{\phi}$ is a scalar (temperature, salinity or CO_2 concentration), D_t is a diffusivity term (m^2/s), and $\hat{n}$ is the number density (m^{-3}) with a source term $\hat{q}$. The subscripts 'd', 'n', 'w', 'CO_2' represent the dispersed phase, the number of bubbles, seawater and CO_2 respectively, with directional vectors represented though the subscripts 'i', 'j', 'k'.

Source terms for mass and momentum exchange terms

In order to solve the governing equations, sub-models for the mass and momentum exchange terms are required:

$$\dot{w}_{co_2} = (6\hat{\alpha})^{1/3}(\pi \hat{n})^{2/3} Sh\, D_f (C - C_0) \quad (1\text{-}17)$$

$$\dot{F} = 0.75\left(\frac{\pi}{6.0}\right)^{1/3} \rho_d \hat{\alpha}^{2/3} \hat{n}^{1/3} C_d \left|u_j - u_{dj}\right|\left(u_j - u_{dj}\right) \quad (1\text{-}18)$$

Eq. (1-17) is the mass exchange from CO_2 dissolution, where Sh is the Sherwood number to calculate the effective mass transfer coefficient, D_f is the CO_2 diffusivity (m^2/s), C is the bubble surface CO_2 concentration (kg/m^3) and C_0 is the seawater CO_2 concentration (kg/m^3). Eq. (1-18) is the momentum exchange term through the drag force between the bubble and the seawater, where C_d is the drag coefficient.

Equations of states for CO_2, seawater and CO_2 enriched seawater

The seawater density at depth is modelled from the international equation of state (UNESCO, 1981), while the density of CO_2 at depth is taken from the data table (M. Ito, 1984). The dispersed CO_2-seawater solution, providing the plume fall down due to density increase, has been modelled from the dissolved CO_2 mass fraction using experimental data by Song et al. (2002), expressed as:

$$\rho_c = (1 + 0.26\chi_S)\rho_w \tag{1-19}$$

pH change of seawater

When CO_2 dissolves in water, it has a chemical reaction where the CO_2 and water mix to produce carbonic acid. The acid and water start to dissociate into bicarbonate ions HCO_3^-, carbonate ions CO_3^{2-}, hydroxide ions OH^- and hydrogen ions H^+ as determined by the international Union of Pure and Applied Chemistry (IUPAC).

$$\begin{aligned} &CO_2 + H_2O \Leftrightarrow H_2CO_3 \\ &H_2CO_3 \Leftrightarrow H^+ + HCO_3^- \Leftrightarrow CO_3^{2-} + 2H^+ \\ &H_2O \Leftrightarrow H^+ + OH^- \end{aligned} \tag{1-20}$$

The number of ions depends on the concentration of the dissolved CO_2, along with their dissociation constants, based on pressure and temperature:

$$\sum CO_2 = \left(\frac{[H^+]}{[H^+] + 2K_2} \right) \cdot \left(1 + \frac{K_2}{[H^+]} \frac{[H^+]}{K_1} \right) \cdot \left([H^+] - \frac{K_w}{[H^+]} \right) \tag{1-21}$$

With $\sum CO_2$ as the total carbon dioxide concentration (mol/l), $K_{i=1,2}$ are the constants for the dissociation of carbonic acid obtained from Saruhashi (1970), and K_w is the ion content of the water suggested by Someya et al. (2005) using data from Marshall and Franck (1981).

The generation of the positive hydrogen ions decreases the pH, meaning that the ocean becomes more acidic (IPCC, 2005). This pH may be calculated through the negative logarithm of the ion content:

$$pH = -Log_{10}(H^+) \quad (1\text{-}22)$$

The change in pH can be estimated through measuring the background pH and the total pH level calculated. The acidity adds to the effect of CO_2 on marine life through large levels causing increased mortality rates, distress and narcosis (IPCC, 2005). Long term, lower levels have an effect on the metabolism of marine organisms causing a detrimental effect on the activity, growth and reproduction of these organisms with fish being slightly less sensitive than marine invertebrates (IPCC, 2005).

Test scenarios run in the North Sea and surrounding waters

Case studies

Case studies have been developed through the use of the oceanic data within the waters, allowing a prediction of leakage scenarios for the selected locations (North Sea: 56.34N, 1.16E, Norwegian Channel: 58.02N, 6.58E, Skagerrak: 58.13N, 9.18E, and West coast: 56.48N, -5.42E). The studies show how the dynamics and dissolution are affected from summer to winter through seasonal data, along with the effect of the leakage depth, tidal currents and initial bubble sizes based on the selected leakage location and the leakage rate, with the various parameters listed in Table 1-2.

North Sea Case Studies	**Depth (m)**	**Leakage Area (m²)**	**Season**	**Leakage Rate (kg/s)**	**Current (cm/s)**
1 – Winter Season	100	15x15	Winter	0.1207	10
2 – Summer Season	100	15x15	Summer	0.1207	10
3 – High leakage rate	100	15x15	Winter	1	10
4 – Low ocean current	100	15x15	Winter	0.1207	1
Localized Waters Case Studies					
5 – Norwegian Channel	320	15x15	Winter	0.1207	20
6 – The Skagerrak	600	15x15	Winter	0.1207	20
7 – Loch Linnhe – Summer Season	20	15x15	Summer	0.1207	5
8 – Loch Linnhe – Winter Season	20	15x15	Winter	0.1207	5

Table 1-2. The set-up data of the case studies.

The case studies one to four show cases modelling the North Sea shelf, mapped at a depth of 100m. Studies five and six take data from the Norwegian Channel, and the Skagerrak at depths of 320m and 600m respectively. Case studies seven and eight compare seasons in a shallow depth leakage prediction from an experiment on the west coast of Scotland (QICS, 2012). The results show 60 mins after a simulated leak occurs, with the leakage rate as suggested by Klusman (2003), as the upper estimate when taking observations from seepage from the Rangely enhanced oil recovery (EOR) field in the USA.

Case study results

In the event of leakage occurring, the questions raised are whether the CO_2 reaches the atmosphere, but also whether there is a substantial increase in CO_2 concentration levels or pH changes of the waters causing harm to the marine environment. The movements of leaked CO_2 or CO_2 solution will also provide information on how or where to detect a leak, providing predictions on the relatively unknown timeframe for detecting leakages.

CO_2 bubbles and droplets plumes

For most of the scenarios, the bubble or droplet plume (with initial sizes of 5.0 ~ 8.0mm) reached their terminal height within the first two and a half minutes of the leakage occurring. This is with the exception of the Skagerrak study, which took a full 30 minutes to reach the terminal height due to the longer distance from the larger mass of droplets and reduced rise velocity from buoyancy.

Reductions in buoyancy force, changes in temperatures and increases in the surface and interface tension between the bubbles, the water and sediments (Espinoza and Santamarina, 2010) overpower the effect of the seawater current, and cause larger initial bubbles at increased depths. This can be seen with the Norwegian Channel case producing larger bubbles than the North Sea shelf, which in turn produces larger bubbles than the low depth leakage off the west coast of Scotland. Fig.1-7 and Table.1-3 show that as the leakage depth increases, the rise height for bubble plumes decreases (west coast over North Sea in Fig. 1-7), with a slower rise velocity from reduced buoyancy overpowering the slightly larger mass of the bubbles at this depth due to fast dissolution with relative larger solubility. However, the rise heights for bubbles with hydrate increase as the greater mass and reduced dissolution rate overpowers the reduced rise velocity. Chen et al., (2009)

found that bubble plume rise heights are more affected by bubble size than depth. However, this can be seen to differ in the case of bubbles with hydrates and droplets with the larger mass increasing the plume height.

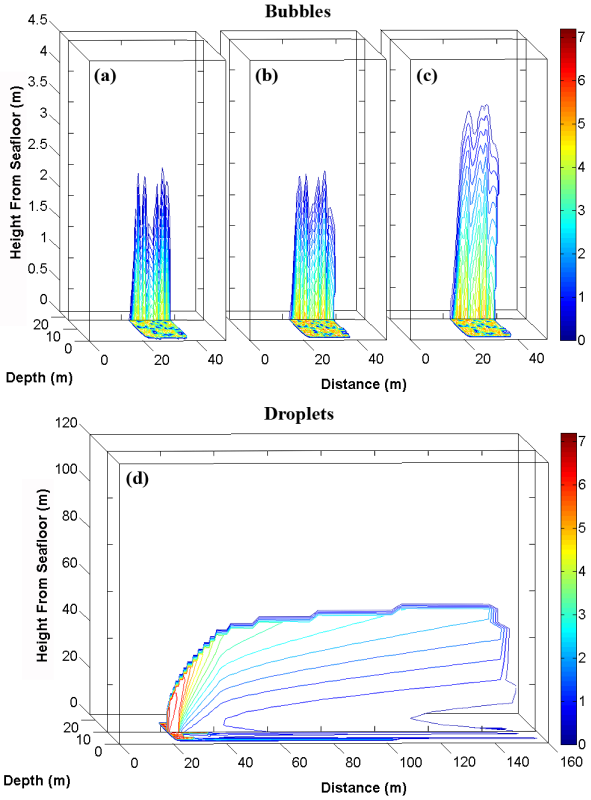

Fig. 1-7. Cross sectional predictions of the rising bubble and droplet plumes of case studies at one hour after leak commences indicated by the bubble/droplet size. (a) The west coast – summer at 20m depth (bubbles); (b) the North Sea shelf – summer at 100m depth (bubbles); (c) the Norwegian Channel – summer at 320m depth (bubbles with hydrates); (d) the Skagerrak – summer at 600m depth (droplets).

North Sea Case Studies	**Maximum Diameter (mm)**	**Dispersed Plume Rise Height (% of depth)**	**Dispersed Plume Rise Height (m)**	**Maximum ΔpH**
1 – Winter Season	5.82	2.81	2.81	-2.03
2 – Summer Season	5.83	2.81	2.81	-2.02
3 – High leakage rate	5.93	2.63	2.63	-2.51
4 – Low ocean current	6.02	3.24	3.24	-2.34
Localized Waters Case Studies				

5 – Norwegian Channel	5.86	1.37	4.38	-1.65
6 – The Skagerrak	7.20	11.87	71.23	-1.09
7 – West coast – summer season	5.77	17.54	3.51	-2.13
8 – West coast – winter season	5.74	15.78	3.16	-2.30

Table – 1-3. The results of leaked bubble/droplet size, plume rising height and maximum changes in pH.

Taking the plume height as a percentage of water depth it can be seen from Table 3 that each study fully dissolves within 31% of the total depth of the waters. Therefore, under these ideal conditions all the CO_2 plumes are expected to dissolve fully before reaching the water surface and atmosphere. However, it should be recognized that the increase in buoyancy could allow the gas to rise further in low depth scenarios, with larger bubble formations from sediments with fine particles or where chimneys form.

Within the North Sea shelf, the changes in season from winter to summer have a negligible effect on the bubble plume height or initial bubble diameters, at this depth there is only around 1°C difference. This is in contrast to shallower depths such as in Loch Linnhe, with the larger temperature differences affecting the densities of the CO_2 and seawater. The increase in leakage rate reduces the plume rise height slightly due to producing a larger number of smaller bubbles with a larger interface area, enhancing the CO_2 dissolution rate of the entire plume as seen in Fig. 1-8 . With the reduced ocean currents, there is an increase in maximum and average bubble diameter forming, increasing the plume height.

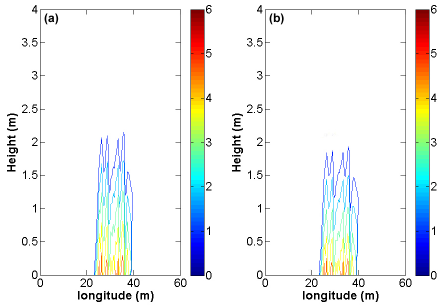

Fig. 1-8. Cross sectional predictions of the rising bubble and droplet plumes of case studies at one hour after leak commences indicated by the bubble/droplet size. (a) the North Sea shelf – winter at 100m depth (bubbles) (b) the North Sea shelf – winter at 100m depth (bubbles) at high leakage rate.

Within the Norwegian Channel, the increase in the depth has the effect of increasing the bubble diameter forming, also providing an increase in rise height when compared to the North Sea shelf as seen in fig.1-7. Due to the increase of mass of the bubbles with depth, the bubbles would take slightly longer to dissolve than in the North Sea cases.

Droplet plume formations such as in the Skagerrak also rise to higher levels than those in the bubble cases. This is in part due to the larger initial droplets forming due to a lower buoyancy force, but the major effect is from droplets having a far greater mass than bubbles of equivalent volume, taking longer to dissolve (Chen et al., 2009). However, due to the large water current in comparison to the rising velocity, the droplet plume travels and dissolves horizontally reducing the overall rising effect from a predicted 165m.

From the low depth bubble scenarios on the west coast of Scotland, and in contrast to the droplet case mentioned previous, the plume height increases due to the larger terminal velocity from buoyancy. When comparing the seasonal changes it can be seen that in winter there is a reduced maximum bubble diameter. The temperature has a larger effect on the density of the seawater (+1.34kg/m^3) than on the CO_2 (+0.124kg/m^3) at low depths; therefore decreasing the temperature increases the buoyancy force providing the smaller initial bubbles and in turn lowering the total rise height of the plume.

Dispersed CO_2 solution plumes

As the CO_2 dissolves in waters, it creates a change in the acidity recorded as a pH change. This solution is higher in density than the surrounding seawater and therefore the plume will drop back to the ocean floor (IPCC, 2005) forcing the largest concentration of pH change and dissolved CO_2 levels at the base near the leak source as seen in Figure 1-9. In Figure 1-10, the volumes of pH change greater than -0.5, -1.0 and -1.5 are recorded within the simulation domain. As can be seen, some of the case study volumes remain relatively constant between the time frames, such as within the Norwegian Channel at 20 minutes, 40 minutes and an hour there is little change in volume to be seen. This is not because there is no increase in volumes of pH change, but is due to the plumes extending beyond the control volume due to the water current.

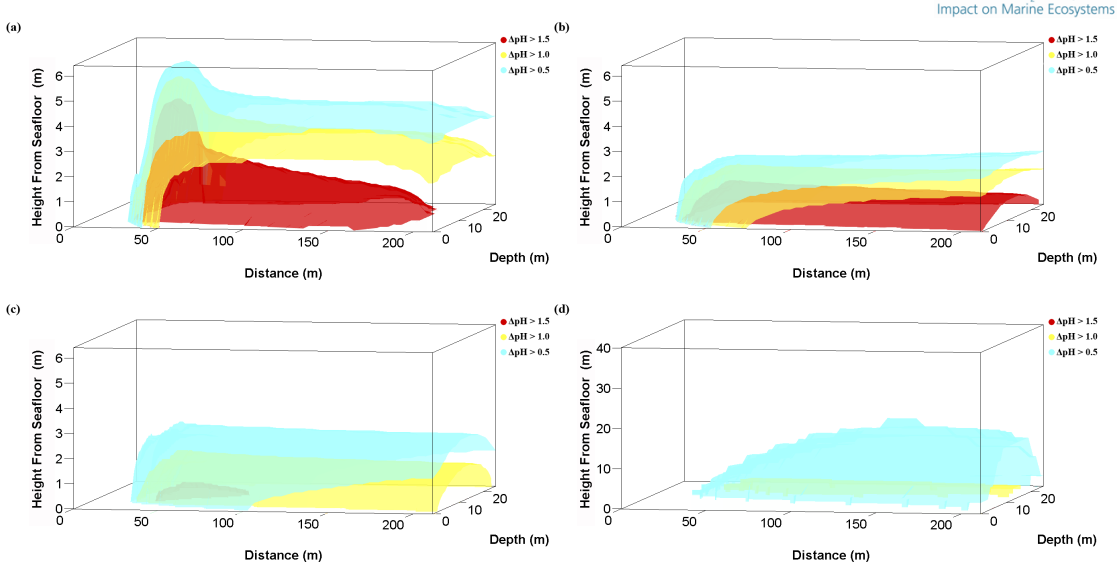

Fig 1-9. Three dimensional prediction of the reduction in pH caused by the dispersed CO_2 one hour after leak commences for changes in pH of greater than -0.5, -1.0 and -1.5. (a) The west coast - summer at 20m depth; (b) the North Sea shelf - summer at 100m depth; (c) the Norwegian Channel - summer at 320m depth (bubbles with hydrates); (d) the Skagerrak - summer at 600m depth (droplets).

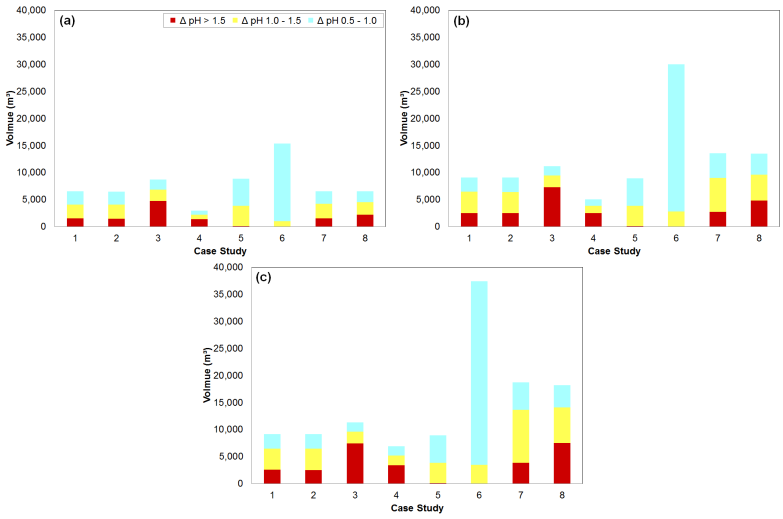

Fig.1-10. The volume of pH concentrations within the carrier plume from each case study, observing a 200 meter horizontal distance for changes in pH of greater than -0.5, -1.0 and -1.5. (a) After 20 minutes; (b) after 40 minutes; (c) after 1 hour.

For the North Sea Shelf, as with the bubble distribution there is a negligible effect of changes in temperature at this depth, with the lower temperature from the winter season creating a slightly larger ΔpH of -0.005 units, and little change in the dissolved solution plume volumes as shown in Fig. 1-10. The increase in leakage rate produces more CO_2

within a similar volume, giving an increase in dissolved CO_2 concentration and maximum change in pH of -2.51 as shown in Table.3. This also provides a larger volume of total and high pH changes (ΔpH > -1.5) shown in Fig. 1-10. A reduction in water current reduces the ability for the plume to distribute horizontally; this therefore also increases the maximum change in pH to -2.34 and the volume of high pH change increases but neither to the same extent as the leakage rate increase.

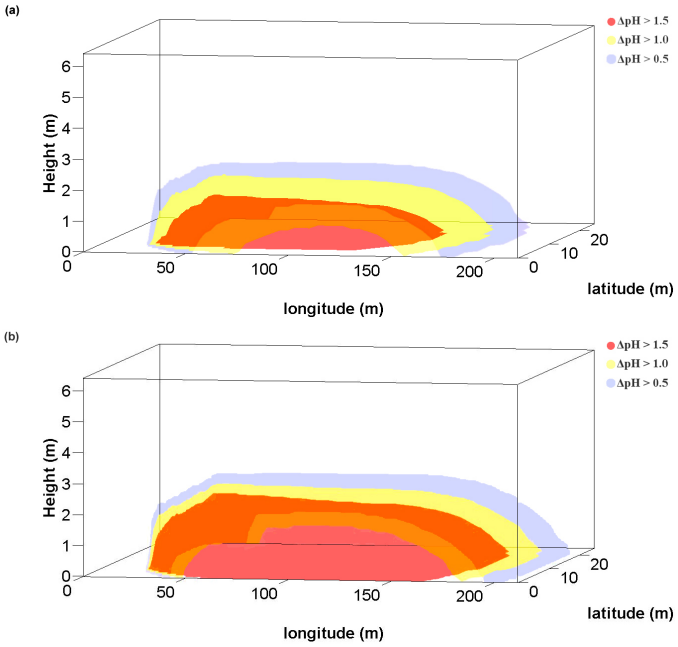

Fig 1-11. Three dimensional prediction of the reduction in pH caused by the dispersed CO_2 one hour after leak commences for changes in pH of greater than -0.5, -1.0 and -1.5. (a) the North Sea shelf – winter at 100m depth (bubbles) (b) the North Sea shelf – winter at 100m depth (bubbles) at high leakage rate.

The increased bubble plume rise height, current and reduced dissolution rate due to the formation of hydrates in the Norwegian Channel distributes the dissolved CO_2 solution giving a reduced change in pH, with little volume of high pH changes, which are 84.69m^3, 85.39m^3, and 85.39m^3 for pH changes larger than 1.5 units at each time frame respectively. However, there is a larger volume of small pH change overall as shown in Fig. 1-10 (a) that extends beyond the simulation domain in the later images due to the high current. Into the Skagerrak, the large droplet plume rise height also distributes the solution, giving a lower change in pH (–1.09) than the lowest North Sea case (–2.02), but a far larger volume

of low pH changes is produced from the droplet rise height, low dissolution rate, and high water currents.

Shallow leakage scenarios such as off the west coast of Scotland provide large volumes of higher pH changes from the reduced water currents, reduced bubble size and high bubble dissolution rate, giving a more concentrated solution. The shallow water, with the large bubble flow rate produces a large relative velocity that is transferred to the seawater through momentum; this generates a wave that carries the CO_2 solution moving vertically. Therefore, in cases 8 and 9, the dissolved solution plume is higher than the bubble plume as shown when comparing Fig. 1-9 (a) with 1-7 (a). In all other cases, the dissolved CO_2 solution plume rises no further than the bubble/droplet leaked plume. Comparing the seasons, again due to the decrease in CO_2 bubble diameter in winter, the bubbles will dissolve quicker providing a further increase in pH change and greater volumes of the larger pH changes.

Summary

Changing individual leakage parameters, such as the depth or current while maintaining other properties across leakage scenarios can have a great affect with clear differences between bubbles and droplets. Droplets have a density at least 100 times that of a bubble of the same volume therefore take more time and distance to dissolve. Due to the lower density of gas, there will be a larger number of bubbles than that of droplets at the same leakage flux, increasing the interfacial surface area enhancing dissolution rates, producing lower terminal heights along with greater pH changes and concentrations. The maximum pH changes are recorded during low current scenarios with high leakage rates and low depth leakage, with the maximum pH change of -2.5 recorded over a 0.04m² grid in the high leakage rate scenario.

These simulations are of a small scale both in time frame and spatial volume, where the buffering through dilution and dispersion based on various currents within the waters have not been taken into account. This would have an effect in longer term analysis of the leak in the larger, meso/regional and global scales, where there is a need to investigate seasonal water-air surface mass transfer directing CO_2 back to the atmosphere and transportation

into deeper waters such as the North Atlantic ocean (Blackford et al., 2008; Bozec et al., 2005; McGinnis et al., 2011; Thomas et al., 2007) and globally (Caldeira and Wickett, 2005).

PART II: MODELLING OF LEAKED CO_2 DISPERSION IN A REGIONAL SCALE

Introduction

This part presents the setup and application of a numerical model of the North Sea using the three-dimensional terrain-following Bergen Ocean Model (BOM) (Berntsen et al. 2000) with 800m-grid resolution. The aim is to demonstrate how the model may be used to simulate transport and dispersion of CO_2 as a passive tracer.

Initial and lateral boundary conditions are taken from the UK Metoffice FOAM 7km model published at http://www.myocean.eu/, so the model is close to being a one way nested submodel of FOAM. The atmospheric forcing data is collected and interpolated from The European Centre for Medium-Range Weather Forecasts (ECMWF, the Centre), "ERA Interim" reanalysis dataset. The tidal forcing is harmonic and currently with 4 tidal constituents. Historical monthly averaged runoffs from approximately 32 European rivers are included. River runoff data comes from a long range of sources assembled during the last couple of decades of modelling efforts, some can be found on the Internet, others from old models developed at the University of Bergen and IMR since the mid nineties. The bathymetry is based on the highest resolution data available from GEBCO (http://www.gebco.net/), with some minor local refinements from previous projects.

Model validation and parameter tuning is on going and currently awaiting data from the summer 2012 cruises. Preliminary current variability data is being fed to the bubble plume models at Heriot-Watt University HWU and GEOMAR, and for point release of CO_2 from the Sleipner area using the output from Heriot Watts plume model as source has been conducted.

Preliminary tests of the spreading of a concentration column of CO_2 with a constant leakage rate have been conducted using different release techniques. A preliminary method for including concentration fields of CO_2 from the bubble plume models at Heriot-Watt University HWU has been devised. (The line source technique described later). The local

current predicted by the ocean circulation model is used for advection of the concentration plume.

Model Description

The flow field computations are performed using the three-dimensional parallel version of the Bergen Ocean Model (BOM). BOM has been in active development since the mid nineties at the Department of Mathematics, University of Bergen, and Uni Research (Bergen), with some contributions from the Institute of Marine Research (IMR). The governing equations solve for the velocity field, pressure, temperature, and salinity, as well as the transport equations for turbulent quantities. BOM is implemented in modern Fortran, and is freely available from http://www.mi.uib.no/BOM/. For further information on BOM, see the user's guide (Berntsen J., 2000).

The governing equations are the Reynolds momentum equations with the Boussinesq approximation and hydrostatic pressure. In the Cartesian coordinates (x,y,z) and time t, these equations are given in the form

$$\frac{\partial U}{\partial t}+\vec{U}\cdot\nabla U-fV=-\frac{1}{\rho_0}\frac{\partial P}{\partial x}+\frac{\partial}{\partial z}\left(K_M\frac{\partial U}{\partial z}\right)+\frac{\partial}{\partial x}\left(A_M\frac{\partial U}{\partial x}\right)+\frac{\partial}{\partial y}\left(A_M\frac{\partial U}{\partial y}\right), \quad (2\text{-}1)$$

$$\frac{\partial V}{\partial t}+\vec{U}\cdot\nabla V+fU=-\frac{1}{\rho_0}\frac{\partial P}{\partial y}+\frac{\partial}{\partial z}\left(K_M\frac{\partial V}{\partial z}\right)+\frac{\partial}{\partial x}\left(A_M\frac{\partial V}{\partial x}\right)+\frac{\partial}{\partial y}\left(A_M\frac{\partial V}{\partial y}\right), \quad (2\text{-}2)$$

$$\frac{1}{\rho_0}\frac{\partial P}{\partial z}=-\frac{\rho g}{\rho_0} \quad (2\text{-}3)$$

and the continuity equation for incompressible fluid

$$\frac{\partial U}{\partial x}+\frac{\partial V}{\partial y}+\frac{\partial W}{\partial z}=0. \quad (2\text{-}4)$$

In these equations $\vec{U}=(U,V,W)$ is the velocity field, U,V and W represent velocities in x-, y- and z-directions, respectively, g is the acceleration of gravity, ρ_0 is the reference density and ρ is the seawater density. The horizontal and vertical viscosity coefficients are A_M and K_M, respectively, which are estimated using a turbulent closure described by Mellor and Yamada 1982. The Coriolis effect, i.e. the effect of the earth

rotation, is accounted for through the two terms on the lhs terms containing the Coriolis parameter.

The conservation equation for tracers, the salinity S and temperature T are expressed as

$$\frac{\partial S}{\partial t}+\vec{U}\cdot\nabla S=\frac{\partial}{\partial z}\left(K_H\frac{\partial S}{\partial z}\right)+\frac{\partial}{\partial x}\left(A_H\frac{\partial S}{\partial x}\right)+\frac{\partial}{\partial y}\left(A_H\frac{\partial S}{\partial y}\right)$$

and

$$\frac{\partial T}{\partial t}+\vec{U}\cdot\nabla T=\frac{\partial}{\partial z}\left(K_H\frac{\partial T}{\partial z}\right)+\frac{\partial}{\partial x}\left(A_H\frac{\partial T}{\partial x}\right)+\frac{\partial}{\partial y}\left(A_H\frac{\partial T}{\partial y}\right)$$

where A_H and K_H are the horizontal and vertical eddy diffusivities. The density is calculated from S and T using an equation of state according to Wang (JPO '84, 1191-1199).

The surface boundary conditions are

$$\rho_0 K_m\left(\frac{\partial U}{\partial z},\frac{\partial V}{\partial z}\right)=(\tau_{0x},\tau_{0y})$$

and

$$\rho_0 K_m\left(\frac{\partial S}{\partial z},\frac{\partial T}{\partial z}\right)=(S_0,T_0),$$

where (τ_{0x},τ_{0y}) is the wind stress vector, while S_0 and T_0 are fluxes of surface salinity and temperature.

The effect of bottom drag on the horizontal velocities is parameterized by

$$\rho_0 K_m\left(\frac{\partial U}{\partial z},\frac{\partial V}{\partial z}\right)=\vec{\tau}_b$$

where $\vec{\tau}_b$ is bottom stress specified as

$$\vec{\tau}_b=\rho_0 C_D\,|(U_b,V_b)|(U_b,V_b)\,.$$

with the bottom drag coefficient

$$C_D=\max\left[0.0025,\frac{\kappa^2}{(ln(z_b/z_0))^2}\right].$$

Here U_b and V_b are the horizontal velocities at the bottom in x- and y-directions, respectively, and the distance of the nearest grid point to the bottom is z_b. The two remaining parameters are the bottom roughness parameter $z_0 = 0.01\text{m}$ and the Von Karman constant, $\kappa = 0.4$.

The dispersion of the CO_2 concentration C is modelled by a similar advection-diffusion equation in the form

$$\frac{\partial C}{\partial t} + \vec{U} \cdot \nabla C = \frac{\partial}{\partial z}\left(K_H \frac{\partial C}{\partial z} \right) + \frac{\partial}{\partial x}\left(A_H \frac{\partial C}{\partial x} \right) + \frac{\partial}{\partial y}\left(A_H \frac{\partial C}{\partial y} \right) \quad \text{2-5}$$

where C is a tracer concentration, and where A_H and K_H are the horizontal and vertical eddy diffusivity coefficients, respectively. It is assumed that the CO_2 concentration is not high enough to cause any significant increase in seawater density, hence is a dynamically passive tracer.

For computing the change in pH due to CO_2 leakage from a sub-seabed CO_2 storage, the software CO2sys.m has been used, (Van Heuven et al. 2011). The input parameters are the total alkalinity (TA = 2054 μ mol/kg-sw), assumed constant and the total dissolved carbon dioxide TCO2, in addition to the temperature, salinity and water depth. When calculating pH change a constant background dissolved inorganic carbon concentration (DIC = 2145 μmol/kg-sw) is added to *C*.

The governing equations given in the Cartesian coordinate system (x, y, z, t) are transformed using terrain-following σ-coordinates (x^*, y^*, σ, t^*), with the following mapping

$$x^* = x, \quad y^* = y, \quad \sigma = \frac{z - \eta}{H + \eta}.$$

Here H is the undisturbed depth and therefore the total depth $D = H + \eta$, η being the surface elevation. The new bottom-following vertical coordinate σ ranges from $\sigma = -1$ at

$z = -H$ to $\sigma = 0$ at the free surface, η. In order to better represent the wind stress at free surface and bottom effects, the sigma-layers are distributed using a profile with denser layers near the free surface and the bottom following (Lynch et al 1995).

The model uses a mode splitting technique, which separates the governing equations into external and internal modes, to step the variables forward in time. The external mode simulates the fast moving surface gravity waves, while the internal mode is for modelling the slow moving internal waves see for example (Berntsen H., 1981), and (Kowalik and Murty, 1993). To compute the external mode, a variant of the depth-integrated equations are used. The full 3D set of equations are not solved as often as the simpler depth integrated equations, therefore the mode splitting technique reduces computational time.

Finite difference/volume methods are used to solve the governing equations on the staggered Arakawa C-grid. The numerical method used for advection of momentum and density is a Total Variation Diminishing (TVD) scheme with a Superbee limiter (Yang and Przekwas, 1992). BOM is parallelized using the Message Passing Interface (MPI), which makes the model suitable for large problems on massively parallel supercomputers.

The effect of Non-hydrostatic pressure has been implemented enabling the model to simulate small-scale physical processes with grid resolutions of less than one meter (Berntsen et al., 2006). The pressure P may be decomposed into three distinct terms: pressure due the surface elevation, $\eta(x,y,t)$, internal pressure and non-hydrostatic pressure $P_{NH}(x,y,z,t)$ (Marshall et al., 1997). Thus

$$P(x,y,z,t) = \rho_0 g\eta(x,y,t) + g\int_z^0 \rho(x,y,\tilde{z},t)d\tilde{z} + P_{NH}(x,y,z,t).$$

However, due to scale of our horizontal resolution, we only use the model in a mode where the hydrostatic assumption is made. This makes the time to solution considerably shorter.
Model setup, forcing and boundary conditions

As a preparation for the scenarios to be performed, BOM has been configured with forcing for the period Jan. 1 - Jun. 30 2012. The period is chosen due to the many ECO2 cruises to

the Sleipner are in summer of 2012. The model forcing data consists of wind, atmospheric pressure, harmonic tides, rivers and initial fields for salinity and temperature. The horizontal grid resolution is 800m and 41 sigma-coordinate layers are used in the vertical, with a vertical resolution of less than 1m in the shallow areas up to tens of meters in the middle of the water column of deep areas.

The model area covers the North Sea in the latitude range from 50 to 64 degrees North. Open boundaries are located at the English Channel and north of the Faroe Island; see Figure 2-1, in order to be as far away from areas of interest as possible.

Initialization and boundary conditions

Water elevation and velocities are spun up from zero. Initial values and lateral boundary conditions of temperature and salinity are taken from the UK Metoffice FOAM 7km model published by MyOCEAN service, at http://www.myocean.eu.org/, and interpolated into the model grid.

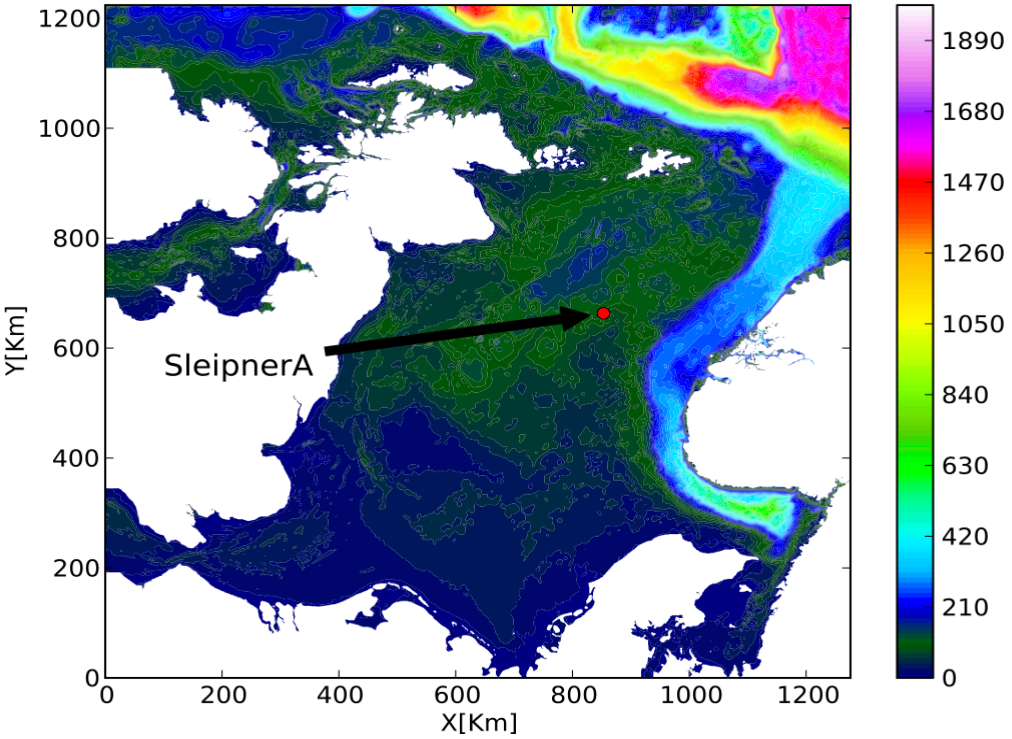

Figure 2-1: The model area covers the North Sea and the colour represents the bathymetry. The model area is located between latitudes 50° N to 64° N and longitudes -12° W to 10° E. The injection point at Sleipner A shown in red is located approximately at (1.9423° E, 58.3635° N).

Lateral boundaries

At the open boundaries the interior solution is relaxed toward an external boundary condition using the Flow Relaxation Scheme (FRS) (Martinsen and Engedahl, 1987) over a relaxation zones of 30 grid cells. In this zone the flow velocity, salinity and temperature is updated at each time step according to

$$\phi = (1-\alpha)\phi_{int} + \alpha\phi_{ext}$$

where ϕ_{int} contains the un-relaxed values computed by the model, and ϕ_{ext} is specified external value. The relaxation parameter α varies smoothly from 1 at the open boundary to 0 at the innermost cell of the boundary zone. The actual external condition from the UK Metoffice FOAM model is interpolated into the model grid once per simulated day.

Tidal forcing

The tidal forcing applied on the open boundaries is taken from harmonic analysis. In the preliminary runs we use four tidal constituents; M2, S2, K1, and N2. Nodal factors and equilibrium arguments needed to get the phase and amplitude right for a given date comes from the ADCIRC model (http://www.adcirc.org/).

Rivers

Fresh water runoff from 32 rivers around the North Sea and Norwegian coast is included. The data is fairly old, originates from the Institute of Marine Research (IMR) and is the monthly mean discharge of the most significant rivers averaged over several years. All rivers contribute water masses with zero salinity and water temperature constant at 10◦C. This temperature is probably too high as an annual mean for most of the rivers, and does not reflect any seasonal variability. This is however the best data available for the river water temperature.

The boundary towards the Baltic Sea has been "closed off" in the model domain but is included as a river discharge through three outlets representing Lillebælt, Storebælt and Öresund. Seasonal variability is obtained by monthly means of water discharge, with realistic salinity and temperature for the Baltic Sea. This method does not allow actual water exchange with the Baltic Sea region, but allows realistic seasonal variation of temperature and salinity in the southern part of Kattegat.

Wind and atmospheric forcing

The wind fields for 2012 are interpolated from the ERA Interim re-analysis dataset from the European Centre for Medium-Range Weather Forecasts (ECMF). These data has a coarse spatial resolution, however the resolution in time is very good and the wind statistics are good. Wind forcing is updated at intervals of 6 simulated hours. Figure 2-2 shows time series of speed and direction from the Sleipner A platform; the red line represents the time-series from ECMWF, the blue line observations from met.no (eklima project web page) and the black line the actually applied interpolated wind inside BOM.

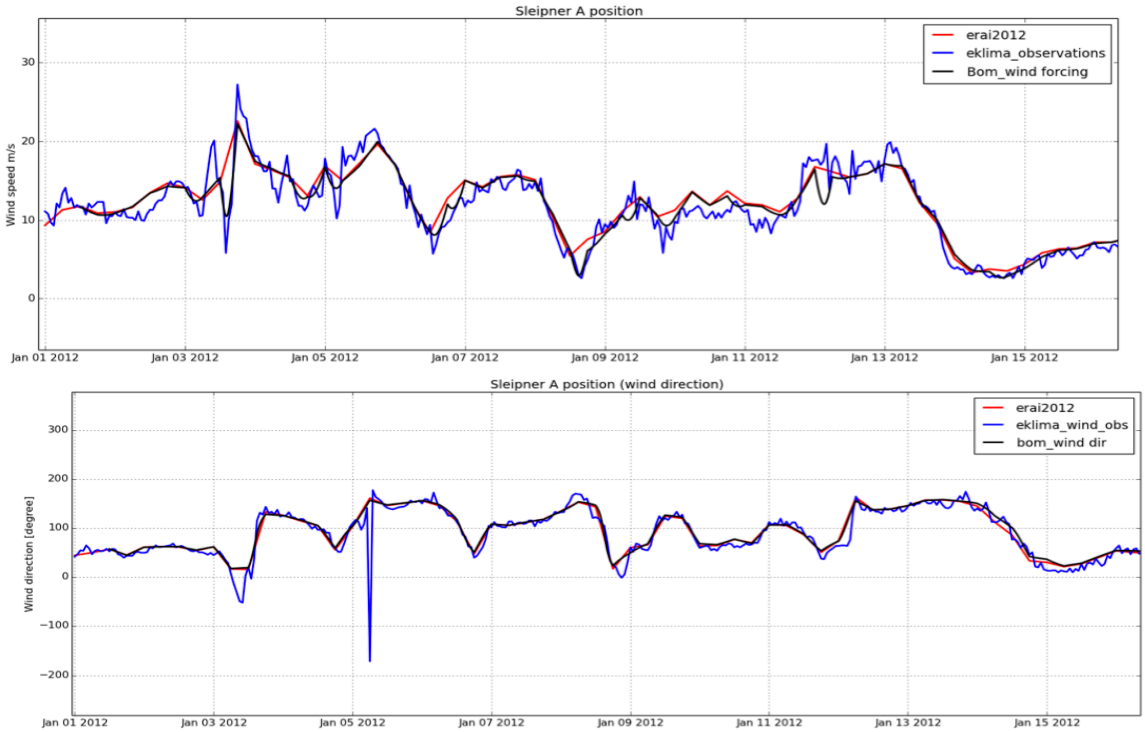

Figure 2-2 Time series of the wind speed (top panel) and wind direction (bottom panel) at Sleipner A in the period J. 01 – 15 2012. Red line represents the data from ERA interim, blue line is the observation from eklima and black line is the interpolated data from ERA-interim 2012 reanalysis in BOM.

Model verification and validation

A number of studies have been conducted to evaluate BOM. One of the first was the work by Berntsen and Svendsen(1999), where a 20km resolution model of the North Sea was compared with the SKAGEX dataset. Avlesen et al (2001) demonstrated grid converged solutions for a geostrophic balance test problem using BOM and the Princeton Ocean Model (POM), verifying the correctness of the basic algorithms for internal pressure and diffusion. In Berntsen et al (2006) BOM is compared to the MITgcm and laboratory experiments for two cases, the lock release problem and the breaking of internal solitary waves in a tank with sloping bottom. A good agreement between models and experiment was found. Thiem et al (2011) simulated the experiments by Carr and Davies (2006), where the step pool method was used to create a two layer stratification and solitary wave, again excellent agreement between model and experiment was found. In Rygg et al (2011), BOM and the MITgcm were again pitted against each other on the flow over backward facing step problem. A convergence study was performed, and numerical results showed

qualitatively good agreement with theory. In a series of papers Berntsen, Xing and Davies (2008,2009,2010) study properties of internal waves at sills in the intensely measured Loch Etive using BOM with non-hydrostatic capabilities, and find very good agreement with measurements and theory, e.g. for the propagation speed of internal waves. Bergh & Berntsen (2009) studied wind generated internal waves and found that growth rate of internal solitons were in good agreement with predictions of steepening timescale from Korteweg-de Vries theory. In a follow up paper (Bergh & Berntsen, 2010) the validity of the surface boundary condition used in BOM was demonstrated through analysing the properties of a surface buoyant jet, where well-known characteristics of the plume front were reproduced.

Validation of the current set up of the model is still on going; especially awaiting release of data from the ECO2 cruises for the summer of 2012. Hence, so far the validation has been to assure that the main features are included in the model. The modelled regional current agrees with the expected surface current patterns in the North Sea, as shown in Figure 2-3 and Figure 2-4. A passive tracer emitted at Sleipner A follows the current in the direction of Skagerak and where after turns and follows the Norwegian coastal current.

A comparison of the modelled tidal elevation with observations at Bergen station is shown in Figure 2-5. The measured data is obtained from http://www.sehavniva.no/. The comparison shows a reasonable agreement with observations regarding the tidal phase, however the discrepancy in amplitude maybe due to the number of constituents and difference in location.

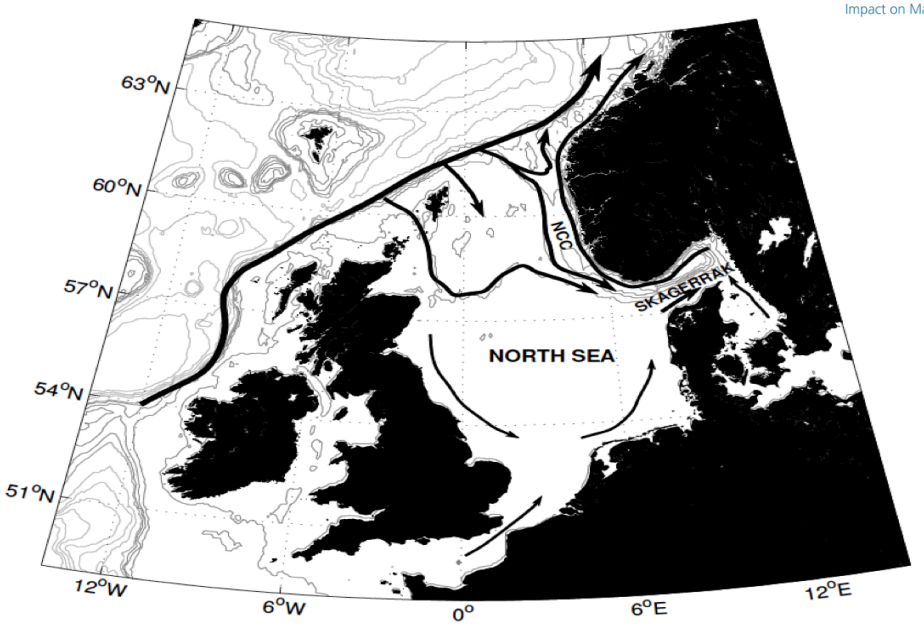

Figure 2-3 Schematic illustration of the main currents in the North Sea (From Østerhus GFI UiB)

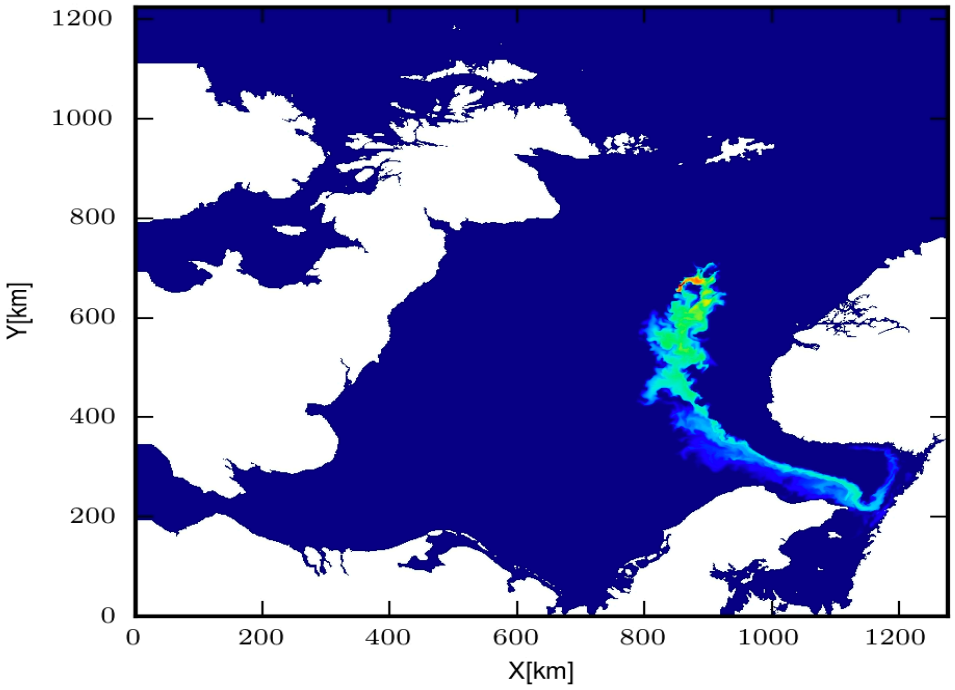

Figure 2-4 Release of a passive tracer at Sleipner A. We observe the tracer follow the observed current pattern from the above figure. The concentration is well below natural variability and detection limits, serves only as an illustration of the regional currents in the area.

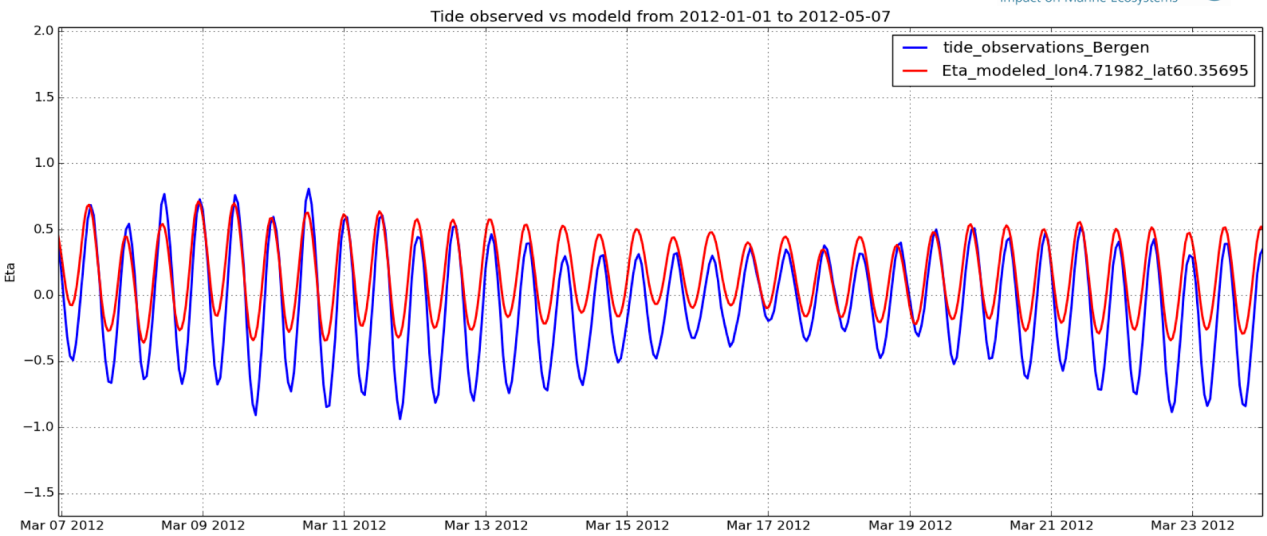

Figure 2-5 Time-series of the modelled tidal elevation at (lon4.719, lat60.357) (red line) compared with observation at Bergen station (blue line). The time period is from 07-24/03/2012.

How model output can assist in impact assessment and monitor design

A validated and reliable general circulation, as the one being used here, can be a valuable tool in all impact assessments and for monitoring design. The most evident use is to simulate transport of CO_2 from a leakage source, as exemplified later. The other is to use model output to fill in gaps in the gathered environmental statistics.

Environmental data sets are often transects during a cruise, and/or time series at fixed locations. Results from a reliable GCM may provide additional insight in the local current conditions, especially filling in gaps both in time and space. Some examples will be given:

The current speed and direction near the free surface (4m depth) and bottom (92 m) at Sleipner are shown in Figure 2-6, which convers the period 01-15/03/2012. In the N-NE direction, the current speed near the surface is approximately twice as strong the near bottom current. Near bottom and surface time-series of the current speed are presented in Figure 2-7. The near seabed current speed is quite similar both in magnitude and variability to measurements we have seen, e.g in the article by (Tryggestad et al 1983). The time series from Tryggestad et al is from Ekofisk, another year and month (August), but is still useful as a comparison, as the deep ocean conditions are not as dependent on season as in the upper layer. We could also observe strong similarity of current amplitude

due to tides. Similarly time series of other environmental variables can be provided, as shown for salinity and temperature in Figure 2-9.

In Figure 2-8, snapshots of the salinity and temperature near the surface at 17/03/2012 are presented. The strong variation in salinity along the Norwegian trench is clearly shown, where the fresh water from the Skagerrak area is mixed with the salt water entering the North Sea from the Atlantic Ocean.

The model has a resolution of 800m which means it can resolve horizontal features of scale approximately 5km. For a location where the current is 0.2m/s, this means a passing eddy will create a time series signal of timescale around 7 hours. The major tidal constituent M2 has a period of around 12 hours, which means the two "noise" signals, eddies and tides, will have a similar signature in the time series.

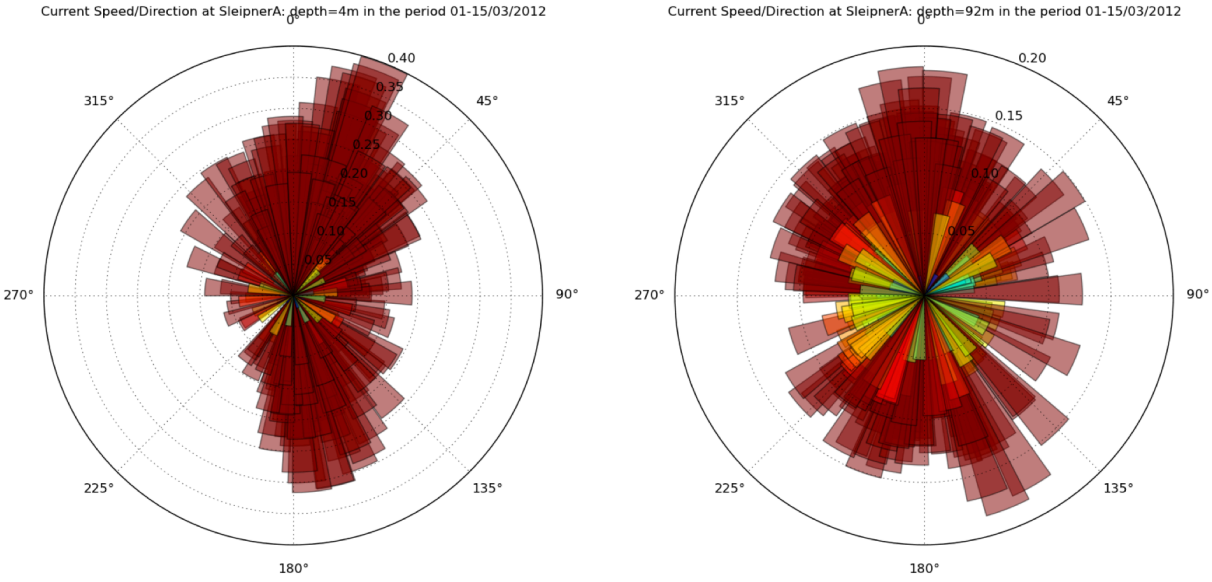

Figure 2-6 Roses of the current speed and direction at Sleipner A point located at (1.9423E, 58.3635 N) in the period 01-15/03/2012. Left panel is at 4 m depth and right panel at 92 m depth and data are sampled every hour

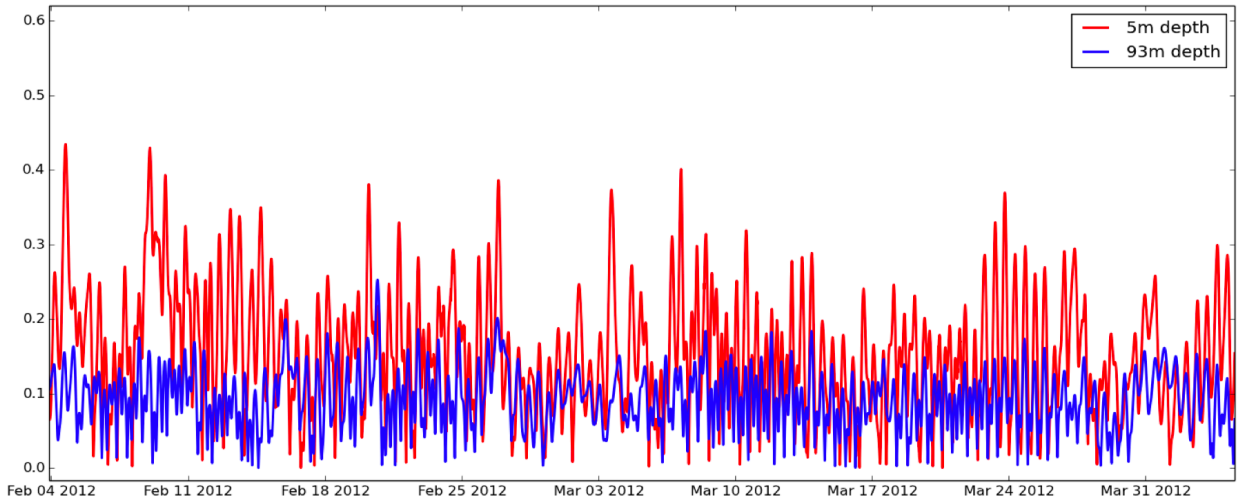

Figure 2-7 Current speed [m/s] at Sleipner A at 5m (red line) and 93 m (blue line).

The temporal variability of salinity and temperature is shown for three depths at Sleipner A in Figure 2-9. The temperature in the deeper part increases with time and become more and more mixed in the vertical towards March 2012.

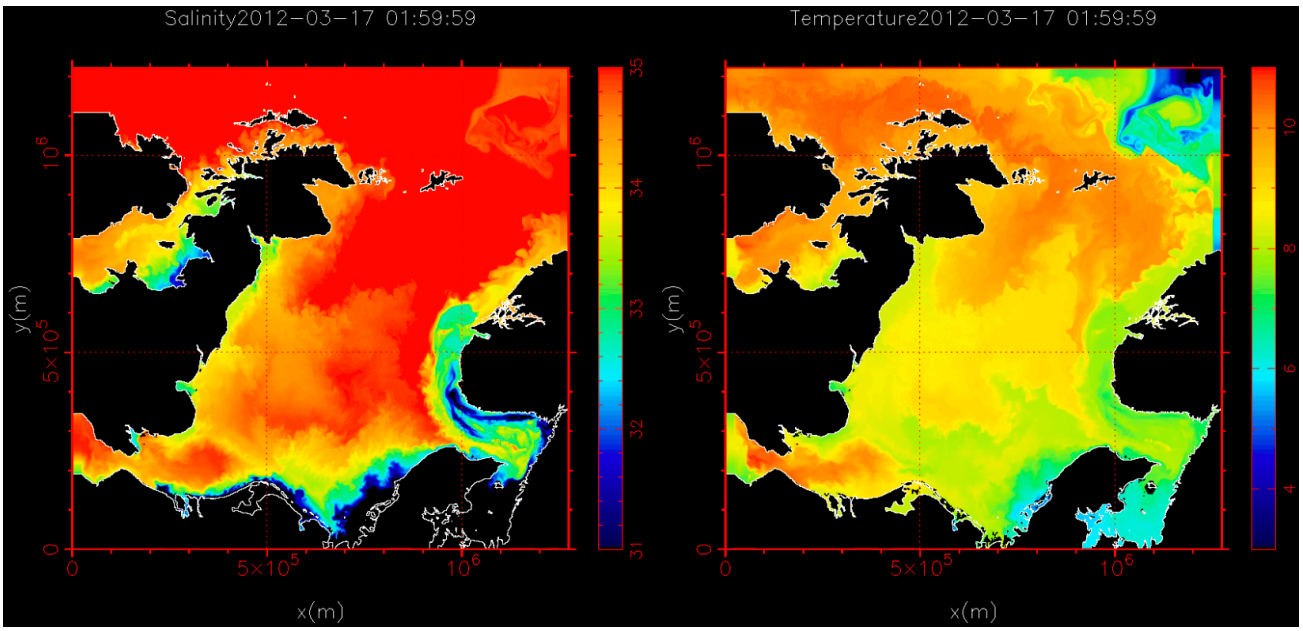

Figure 2-8 Snapshot of the salinity (left) and temperature (right) profiles at 2012-03-17 01:59:59 at 5m depth.

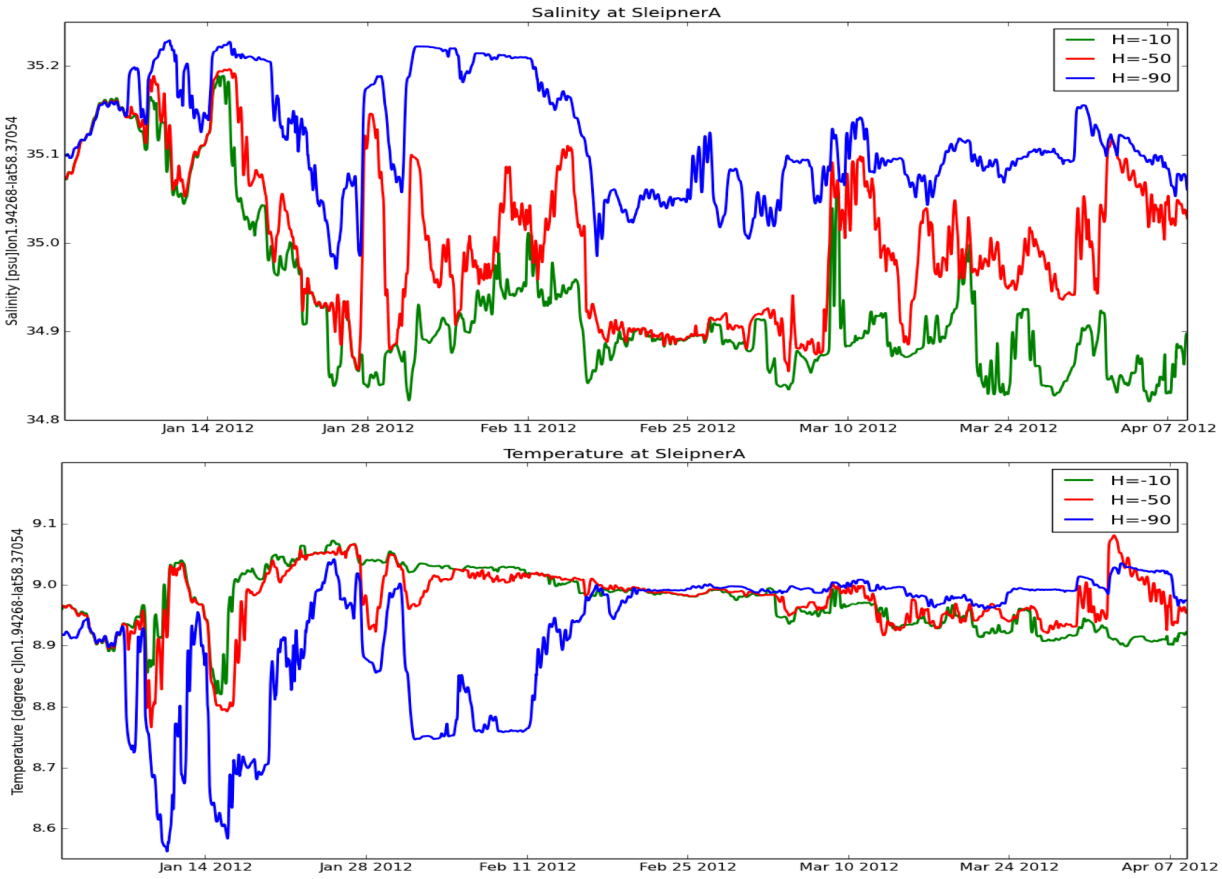

Figure 2-9 Time-series of salinity (top panel) and temperature (bottom panel) at Sleipner A, at depths of 10m (green line), 50m (red line) and 90m (blue line). The period is from Jan. 01- Apr. 07 2012.

Demonstrating of transport and dispersion of CO_2

This section goes a bit further and present the results of the initial dispersion and transport of CO_2 plume, leakage scenarios at the Sleipner A injection point located at (1.9423° E, 58.3635° N). The model setup does not simulate the process of the CO_2 bubble dissolving in the water column; however the model considers the spread and transport of the dissolved CO_2 as a tracer concentration through an advection-diffusion equation. In the next three subsections we present three methods for including a source of CO_2 from the seafloor.

Box method

In this method, the CO_2 concentration is directly set and updated in a box of volume 800.0 $\times 800.0 \times 10.0\, m^3$ located near the seabed at Sleipner A. Then the CO_2 is advected by the diffusion-advection equation. For instance, the leakage rate is 0.1 kg s^{-1} leads to the leakage flux $Q = 0.1/(800.0 \times 800.0 \times 10.0)$ kg $m^{-3} s^{-1}$. Then the concentration C is updated inside this box at every time step by

$$C_{n+1} = C_n + Q \times \Delta t .$$

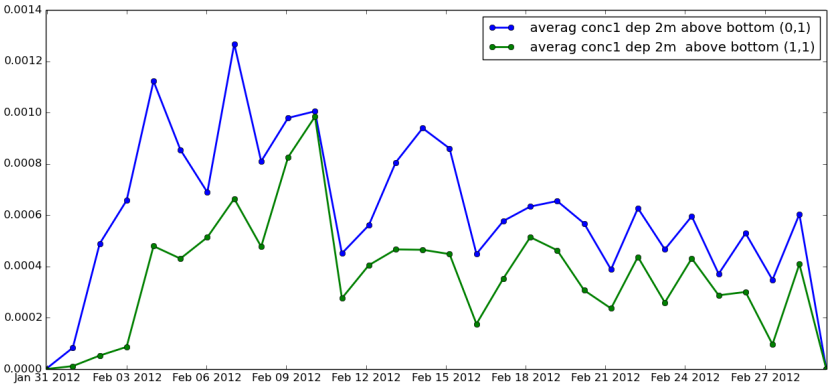

Figure 2-10 Daily averages of concentration 2m above the sea floor of a passive tracer released at Sleipner A. The sample points are near the release point and 800m to the northeast.

The daily variability of the concentration can be seen in Figure 2-10 as two time-series of daily averaged concentration 2m above the sea floor. The sample points are at the release point (blue line) and at 800m north-east (green) of the release point. Figure 2-11 illustrates how the normal values of the concentration deviate from its daily average. Figure 2-12 shows the time series of wind speed for the same time period as the concentration time series of Figure 2-10 and 2-11. We observe that there may be a correlation between high wind speed events and increased concentration.

Results from using the box method are presented in Figure 2-13, where the total run time is about two months. Due to the main current pattern in the North Sea, we observe that CO_2 is transported towards Skagerrak, the concentration, however, is not measurable as the released CO_2 is quickly diluted in the large volume of water.

An import impact due to CO_2 leakage into the water column is the water acidification and reduction in pH. Therefore, it would be interesting to present results on the change in pH. In this regard, the background dissolved inorganic carbon (DIC = 2145 μmol/kg-sw) and the total alkalinity TA= = 2054 μmol/kg-sw are used to calculate the background pH. The dissolved CO_2 in kg/m^3 is converted to μmol/kg-sw using the conversion: 1 kg/m^3 = 22722.37 μmol/kg-sw , and then added to background DIC. Therefore the sum is passed in the input to the program CO2sys to calculate change in pH. As shown in Figure 1-14, the maximum pH change occurs near the leakage and reaches about 0.01, which is below the natural variability. When we zoom in in Figure 2-14 around the area of the pH change, it can be seen that the dispersion of the plume is very much affected by the variability in the water currents.

For the near field plume dispersion in the water column (for about two months run starting March 1), two vertical cross-sections touching the artificial leakage point at Sleipner A, are shown in Figure 2-15, in the left panel we look in the positive *y* direction, the right panel we look in the negative *x* direction. The figure again demonstrates that the dispersion of the plume is mainly eastward towards the Norwegian trench. In the other panel, we observe the dispersion in y direction is similar in the negative and positive direction.

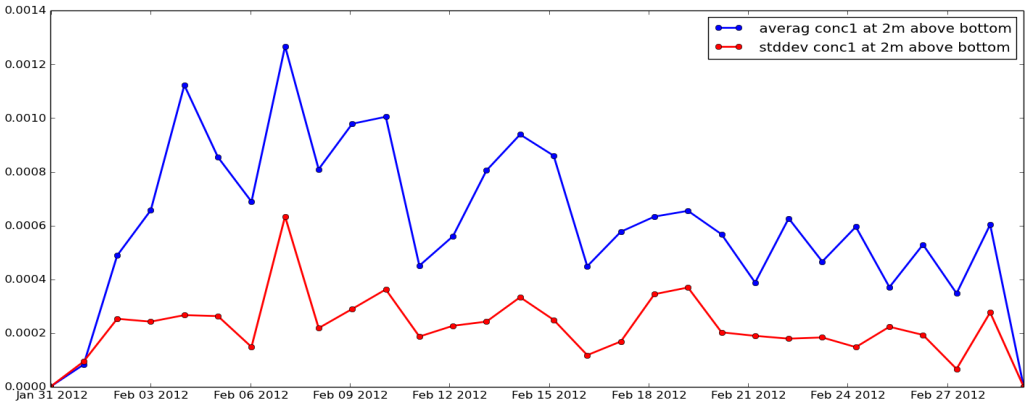

Figure 2-11: The blue line shows a time-series of the daily averaged concentration and the red line is the corresponding standard deviation at 2m above the sea floor, near the artificial release point at Sleipner A.

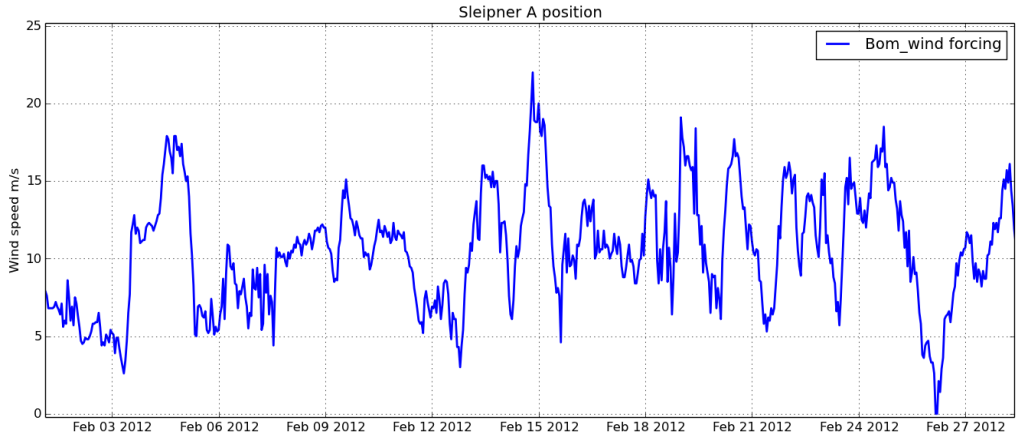

Figure 2-12 Time series of wind speed at 10m heights for Sleipner A from the same time range as the time series for concentration in Figure 2-11.

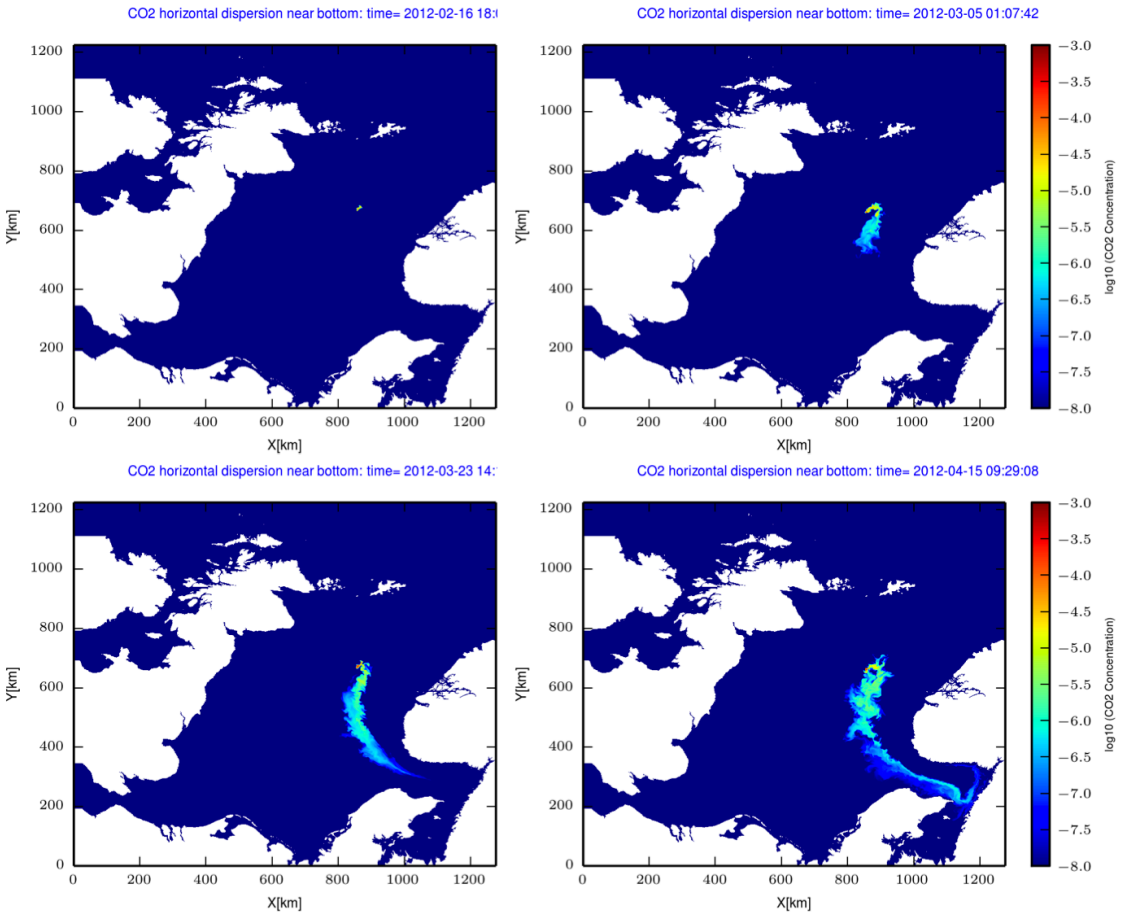

Figure 2-13 Snapshots of the dispersion of CO_2 concentration field leakage implemented using the box method. The flux leakage rate is 0.1/(800.0x800x10.0) kg/m^3/s, and the colour is in logarithmic scale. The runtime is about two month starting Feb. 15 2012.

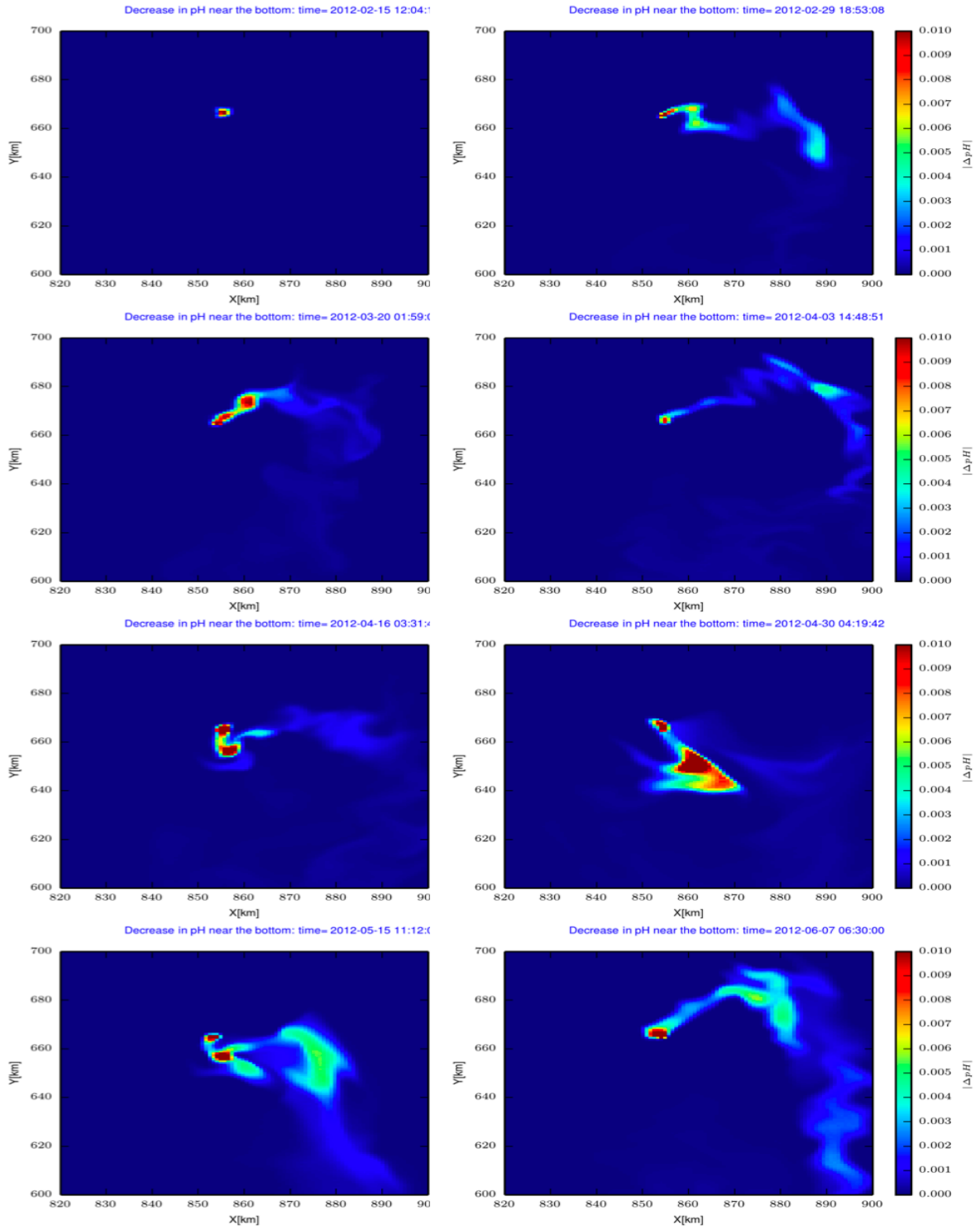

Figure 2-14 Near-bottom pH change due to leakage of CO_2 results from Figure 2-**13, using the carbon system tools CO2sys.m. The figures show a closer look at the area around the leakage point.**

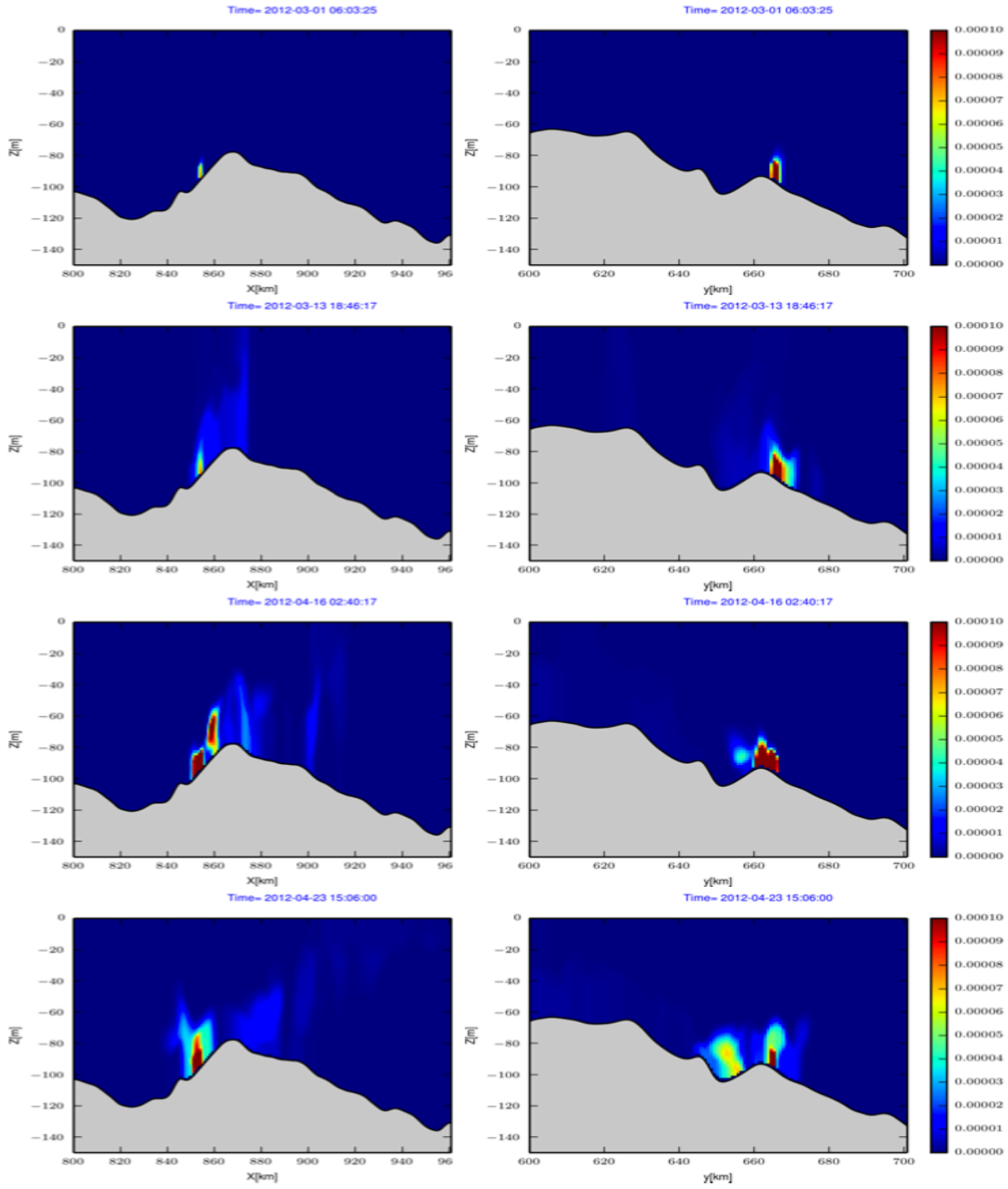

Figure 2-15 The snapshots show the dispersion of the concentration on vertical cross sections along x-direction (left) and y-direction (right) that cross the leakage point. The release of the concentration starts 01/03/2012.

Line source method

Another method that has been implemented in our model is a vertical line source, where the concentration field is given as input files and prescribed to be the solution in a vertical

line of the domain, much in a similar manner as a lateral boundary condition. The prescribed concentration is then advected horizontally with the currents. This method is an example of how output from a small-scale bubble/plume model can be included in a general circulation model.

As input we use the preliminary CO_2 concentration field obtained from a two-phase small-scale bubble plume model from Heriot-Watt University. The volume of this model is $800.0 \times 4.77 \times 800.0\, m^3$, and the leakage rate is approximately 0.12 kg/s. The CO_2 is leaked in the form of bubbles over an area of 15x15 m^2, therefore the flux rate is 5.36E-04 $kg\ s^{-1}\ m^2$. The steady state solution is taken as input to our large-scale model through the so-called line source method. The results of the near-bottom plume dispersion are shown in Figure 2-16. The CO_2 plumes propagate into the Skagerrak, with the current, and while the concentration has a very small, immeasurable magnitude, it is included to visualize how fluid parcels from the release point are transported.

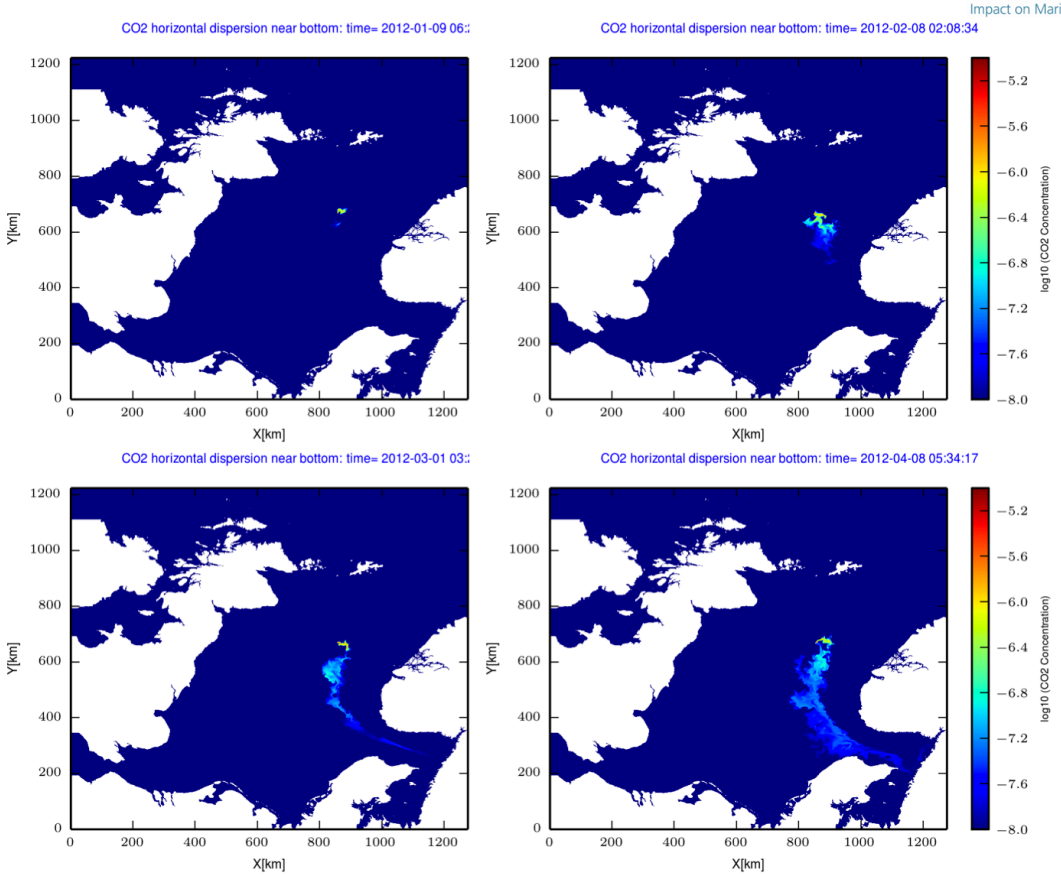

Figure 2-16 Near bottom advection of CO_2 concentration field. The steady initial solution is taken from a smal-scale model by HWU and implemented as input field using line method source.

Well method

In the well method implemented in BOM, water with dissolved CO_2 is leaked from a single grid cell of area 800x800 m^2. The CO_2 concentration C in kg m^{-3} and the water volume flux Q in m^3 s^{-1} can be constant or time varying. Consequently the leakage rate will be $C*Q$ in kg s^{-1}. For testing this method, four experiments were performed in which the leakage rate is fixed to 0.1 kg/s, however C and Q are changed as in Table 2-1. Two scenarios of low volume flux with high concentration and high volume flux with low concentration were investigated.

Table 2-1: Values of the initial concentration C and volume flux Q for the four experiments performed using the Well method, in which the CO_2 is emitted through a well in a form of CO_2-enriched water.

	C [kg m^{-3}]	Q [m^3 s^{-1}]
Ex1 (Figure 2-17)	0.1	1
Ex3 (Figure 2-18)	0.001	100

In EX1 and EX2, the leakage rate is fixed to 0.1 kg s^{-1}, but C and Q are changed to investigate the area affected and the dynamic of spreading of the CO_2 plume. The results (see Figures 2-17 and 2-18) show the footprint of the dissolved CO_2 plume after two months run time. It can be observed that the affected area in EX1 is approximately around the leakage point. In Ex2 the area is extended further south, even though the leakage rate is the same. This difference is due to the difference in volume flux through the leakage point, which has an effect on the dispersion of CO_2. By comparing dispersion from a numerical experiment using the well method with real experiments or high resolution bubble plume models, it may be possible to find a model for specifying the well method volume flux in a way that balances vertical advection and diffusion of CO_2 and gives the best agreement.

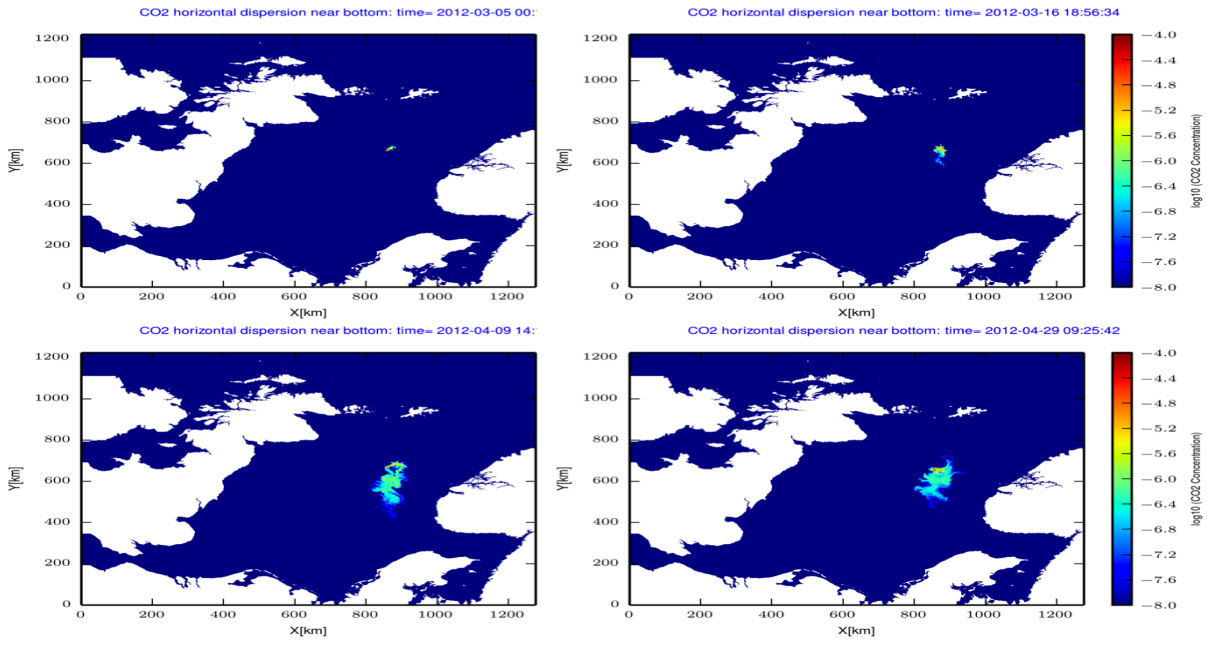

Figure 2-17. Advection of CO_2 concentration field near the seabed, using the Well method. The CO_2 concentration $C =$ 0.1 kg m^{-3} and leakage flux $Q =$ 1 m^3 s^{-1} (EX1), , and the color is in logarithmic scale. The runtime is about two months starts 2012-03-01 12:00:00.

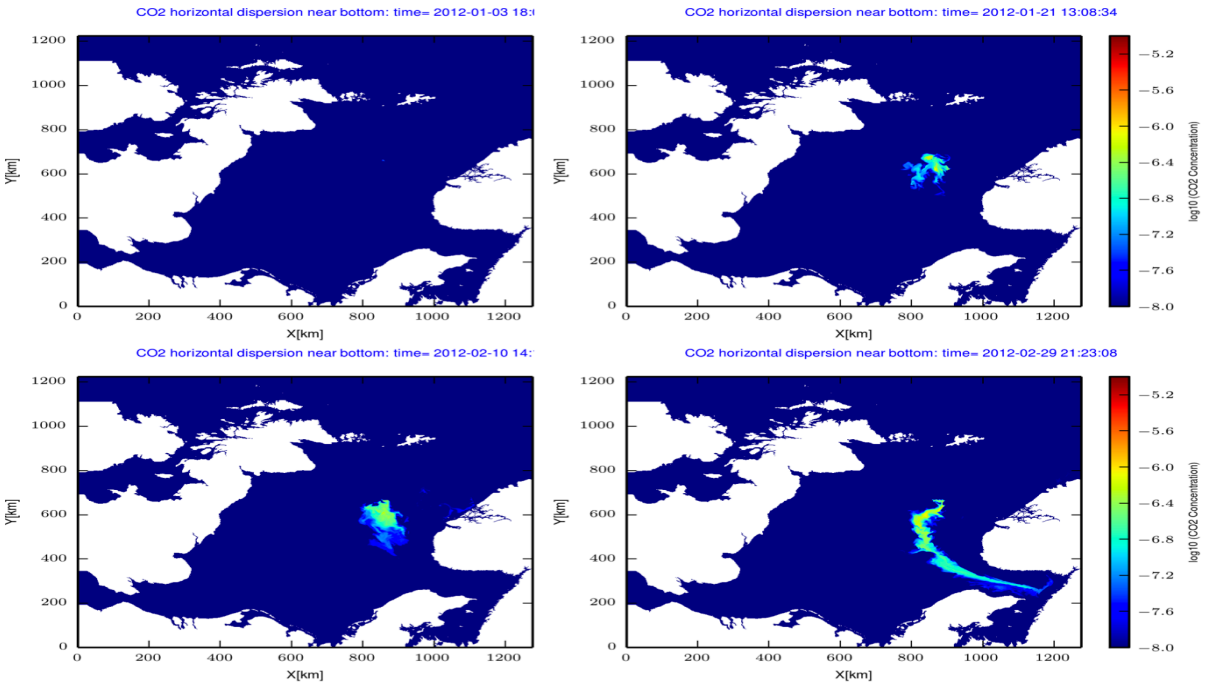

Figure 2-18 Advection of ***CO_2*** concentration field near the seabed using the Well method. The CO_2 concentration $C =$ 0.001 kg m^{-3} and leakage flux $Q =$ 100 m^3 s^{-1} (EX2) ***and the colour is in logarithmic scale***, starting at 2012-01-01 12:00:00.

Summary

Bergen Ocean Model, a three-dimensional regional ocean model system, has been set up for the North Sea with 800m horizontal grid resolutions. The model system currently has forcing data for 2012, and is driven with 4 tidal constituents and climatological river runoff from the major rivers in the domain. Results reproduce well-known features of the currents in the North Sea. The modelled tidal elevation has been compared with measurements at a few selected locations and show reasonable agreement. Validation against measurements from ECO2 cruises is pending access to data.

Initial testing of various techniques for modelling dispersion of CO_2 released from point sources show that the concentration of CO_2 for small leakage rates quickly fall below the natural variability and detection limits. However it is demonstrated how the model set up can provide statistics for impact assessments and for designing a monitoring program.

PART III: MODELING OF MARINE CHEMISTRIES AT THE SEDIMENT-WATER INTERFACE

INTRODUCTION

This report presents the setup and application of a numerical model of the biogeochemical processes at the sediment-water interface. CO_2 leakage origin carbon should be involved into biogeochemical transformations in the pore water of the sediments and in the bottom boundary layer (BBL). From one side, this excessive carbon should affect the distributions of other chemical parameters, and from the other side, it should change its concentrations and properties. These transformations should significantly depend on the sediment water interface redox conditions, that are connected with some other factors (i.e. amount and quality of the organic matter, water column mixing) that are characterized by significant temporal (first of all seasonal) variations. The goal of this work was to elaborate a model capable to describe the basic biogeochemical processes occurring at the sediment-water interface and to apply this model for the Sleipner case. This model will increase our ability to perform risk assessments should a leak occur.

This study investigates modeling of biogeochemical transactions between sediment and bottom water. We use a 1-dimensional C-N-P-Si-O-S-Mn-Fe vertical transport-reaction model describing both the sediments and bottom boundary layers coupled with biogeochemical block simulating changeable redox conditions, and the carbonate system processes block. The main focus of this investigation relates to the Bottom Boundary Layer, the most active zone of interactions. Organic matter formation and decay, reduction and oxidation of species of nitrogen, sulfur, manganese, iron, and the transformation of phosphorus species are parameterized in the model.

MODEL DESCRIPTION

In the frames of the project we merged the existing biogeochemical models (ROLM, OxyDep, CO2SYS) and elaborated a new 1-dimensional C-N-P-Si-O-S-Mn-Fe vertical

transport-reaction model that describes the processes in the water column, bottom boundary layer and benthic boundary layer with biogeochemical block simulating redox conditions changeability (the Bottom RedOx Model, BROM, Fig. 3-1).

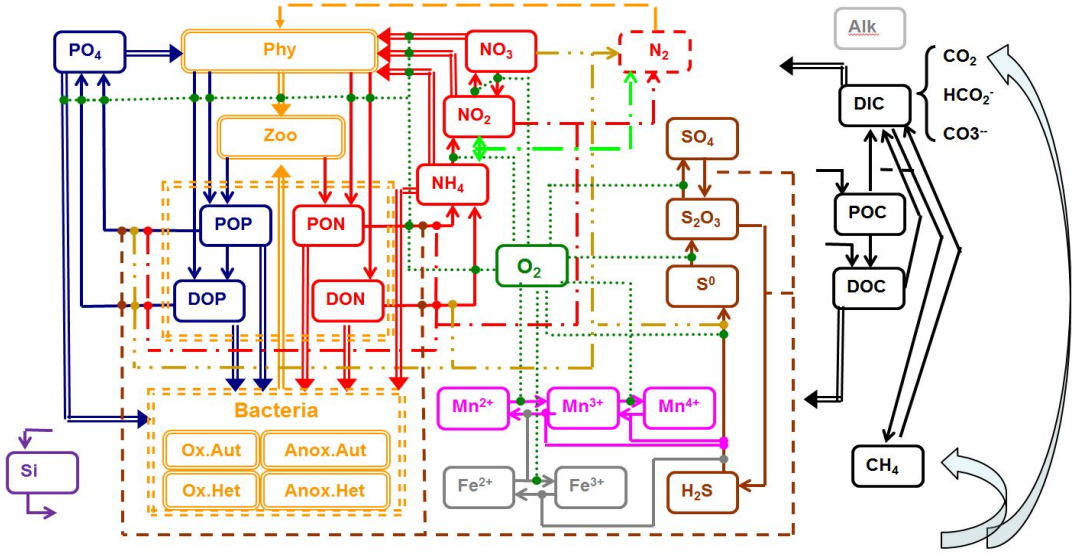

Fig. 3-1. Flow-chart of biogeochemical processes represented in the Bottom RedOx Model (BROM).

The elaborated for the water column processes biogeochemical model ROLM (RedOx Layer Model) allowed to simulate basic features of biogeochemical structure changes in oxic, anoxic and changeable conditions (Yakushev et al., 2007). ROLM was applied for the description of the oxic/anoxic interface structure and estimation of the process rates in the Black and Baltic Seas (Yakushev et al., 2009, 2011, He et al, 2012) and to study the consequences of the oxygenated intrusions into the anoxic layers (Yakushev et al., 2011). This chemical processes model was coupled with 1D transport model model GOTM (Yakushev et al., 2009), and 3D hydrodynamical model GETM (He et al., 2012). The simplified biogeochemical model OxyDep (Biota-Dissolved Organic-Matter – Particulate Organic Matter – Nutrient -Oxygen), coupled with a standard model for description of the carbonate system balancing CO2SYS (Lewis and Wallace, 1998) was used for the Barents Sea modelling (Yakushev, Sørensen, 2013).

In BROM we parameterized organic matter (OM) formation and decay, reduction and oxidation of species of nitrogen, sulfur, manganese, iron, and the transformation of

phosphorus, silicate and carbon species. BROM includes a simplified ecological model with phytoplankton, heterotrophic organisms, aerobic autotrophic and heterotrophic bacteria, anaerobic autotrophic and heterotrophic bacteria (Fig. 3-1). Carbonate system equilibration is modeled using CO2SYS (Lewis and Wallace, 1998). This version of the model is written in MATLAB.

The time space evolution of the model compounds variables is described by a system of horizontally integrated vertical diffusion equations for non-conservative substances:

$$\frac{\partial C_i}{\partial t} = \frac{\partial}{\partial z} K_Z \frac{\partial C_i}{\partial z} - \frac{\partial((W_C + W_{Mn})C_i)}{\partial z} + R_{C_i} \qquad (3\text{-}1)$$

$$R_{C_i} = \sum_j Rate_{BjC_i}$$

where C_i - concentration of a model compounds; K_z - vertical transport coefficient; W_C is the sinking rate of the particulate matter; W_{Mn}, - accelerated rate of sinking of particles with settled Mn hydroxides; Rci- sources and sinks of a substance (rates of transformation), being a algebraic sum if local fluxes caused by biogeochemical interaction ($Rate_{BjCi}$).

The following parameters (C_i) were considered in the model: Dissolved oxygen (O_2), hydrogen sulfide (H_2S), total elemental sulfur (S^0), thiosulfate (and sulfites) (S_2O_3), sulfate (SO_4), ammonia (NH_4), nitrite (NO_2), nitrate (NO_3), particulate organic nitrogen (PON), dissolved organic nitrogen (DON), phosphate (PO4), particulate organic phosphorus (POP), dissolved organic phosphorus (DOP), dissolved reduced manganese (MnII), dissolved oxidized manganese (MnIII), particulate oxidized manganese (MnIV), dissolved reduced iron (FeII), particulate oxidized iron (FeIII), phytoplankton (Phy), zooplankton (Zoo), aerobic heterotrophicbacteria (B_ae _het), aerobic autotrophic bacteria (B_ae_aut), anaerobic heterotrophic bacteria (B_anox _het), alkalinity (Alk), total inorganic carbon (TIC) and silisca (Si). Data on temperature, salinity, Alk and TIC where used for calculations of the carbonate system parameters.

In general, the parameterization of rates of the biogeochemical interactions, $Rate_{BG,}$ is as follows:

$Rate_{BG} = K_{BG}\ Dep_{re1}\ Dep_{re2}\ [Dep_{inh}]$

where K_{BG} is a constant; Dep_{re1} is a dependence on concentration of the 1st reacting variable; Dep_{re2} is a dependence on concentration of the 2st reacting variable, and Dep_{inh} is a dependence on concentration of a variable that inhibits the reaction.

A simplest linear dependence (such as the first order kinetics) is appropriate for the reactions of substances that coexist in small concentrations as O_2 and H_2S or NO_3 and FeII). non-linear dependence with "switches" (quasi-linear, Michaelis-Menten in different modifications, hyperbolic tangents) in situations when the concentrations of the considered substances differed significantly or were mediated by biological organisms (for instance a description of a switch between oxic OM decay and denitrification).

There can be also added a function of inhibition as an additional switch to describe, for instance, a switch between the reactions in suboxic and anoxic conditions.

A list of the biogeochemical processes considered is given in Table 3-1.

Table 3-1. Parameterization of biogeochemical processes.

Name of Process / reaction	Parameterizations
Autolysis	$AutolisP=K_{PD}\ POP$ $AutolisN=K_{PD}*PON$
Mineralization at oxic conditions $(CH_2O)_{106}(NH_3)_{16}H_3PO_4 + 106O_2 = 106CO_2 + 16NH_3 + H_3PO_4 + 106H_2O$	$DcDM\_O2=exp(Ktox*T)*K_{ND4}*DON*Fox$ $DcPM\_O2=exp(Ktox*T)*K_{NP4}*PON*Fox$ $Fox = \begin{cases} = 0 & for\ O_2 \le O_2ox \\ = \dfrac{(O_2 - O_2ox)}{(O_2 - O_2ox + Kox)} & for\ O_2 > O_2ox \end{cases}$

Denitrification $(CH_2O)_{106}(NH_3)_{16}H_3PO_4 + 84.8HNO_3 = 106CO_2 + 42.4N_2 + 148.4H_2O + 16NH_3 + H_3PO_4$ $1/2CH_2O + NO_3 \rightarrow NO_2^- + 1/2H_2O + 1/2CO_2$ $3/4CH_2O + H^+ + NO_2^- \rightarrow 1/2N_2 + 5/4H_2O + 3/4CO_2$	$Denitr1\_PM = K_{N32} * Fdnox * FdnNO3 * PON$ $Denitr2\_PM = K_{N24} * Fdnox * FdnNO2 * PON$ $Denitr1\_DM = K_{N32} * Fdnox * FdnNO3 * DON$ $Denitr2\_DM = K_{N24} * Fdnox * FdnNO2 * DON$ $Fdnox = \begin{cases} = 0 & for\ O_2 > O_2dn \\ = 1 - \frac{O_2}{O_2dn(O_2dn + 1 - O_2)} & for\ O_2 \le O_2ox \end{cases}$ $FdnNO3 = \begin{cases} = 0 & for\ NO_3 \le NO_3mi \\ = 1 - \frac{NO_3 - NO_3mi}{NO_3 - NO_3mi + 1} & for\ NO_3 > NO_3mi \end{cases}$ $FdnNO2 = \begin{cases} = 0 & for\ NO_2 \le NO_2mi \\ = 1 - \frac{NO_2 - NO_2mi}{NO_2 - NO_2mi + 1} & for\ NO_2 > NO_2mi \end{cases}$ $DcPM\_NO_3 = Denitr1\_PM + Denitr2\_PM$ $DcDM\_NO_3 = Denitr1\_DM + Denitr2\_DM$
Sulfatereduction $(CH_2O)_{106}(NH_3)_{16}H_3PO_4 + 53SO_4^{2-} = 106CO_2 + 106H_2O + 16NH_3 + H_3PO_4 + 53S^{2-}$	$s4\_rd\_PM = K\_s4\_rd\ Fsox\ Fsnx\ SO_4\ PON$ $s4\_rd\_DM = K\_s4\_rd\ Fsox\ Fsnx\ SO_4\ DON$ $s23\_rd\_PM = K\_s23\_rd\ Fsox\ Fsnx\ PON\ S_2O_3$ $s23\_rd\_DM = K\_s23\_rd\ Fsox\ Fsnx\ DON\ S_2O_3$ $Fsox = \begin{cases} = 0 & for\ O_2 > O_2sr \\ = 1 & for\ O_2 \le O_2sr \end{cases}$ $Fsnx = \begin{cases} = 0 & for\ (NO_3 + NO_2) > Nosr \\ = 1 & for\ (NO_3 + NO_2) \le Nosr \end{cases}$ $DcPM\_SO_4 = s23\_rd\_PM + s4\_rd\_PM$ $DcDM\_SO_4 = s23\_rd\_DM + s4\_rd\_DM$
Ammonification and phosphatification	$AmmonPON = DcPM\_O_2 + DcPM\_NO_3 + DcPM\_SO_4$

	$AmmonDON=DcDM\_O_2+DcDM\_NO_3+DcDM\_SO_4$ $PhosPOP=AmmonPON/16$ $PhosDOP=AmmonDON/16$
Nitrification $NH_4^+ + 1.5\ O_2 \rightarrow NO_2^- + 2H^+ + H_2O$ $NO_2^- + 0.5\ O_2 \rightarrow NO_3^-$	$Nitrif1=K_{N42}*NH_4*O_2/(O_2+O_2nf)$ $Nitrif2=K_{N23}*NO_2*O_2/(O_2+O_2nf)$
Nitrogen fixation	$Nfixation = K_{Nfix}^{\max} \frac{1}{1+\left(\frac{NO_3+NO_2+NH_4}{16PO_4}\right)^4} \frac{PO_4}{PO_4+0.3} K_{NF} \cdot f_i(i) \cdot f_t(T) \cdot Phy \cdot Sn$
Anammox $NO_2+NH_4 \rightarrow N_2+2H_2O$	$Anammox= NO_2*NH_4*K_{annamox}$
Oxidation of reduced S forms with oxygen $2H_2S + O_2 \rightarrow 2S^0 + 2H_2O$ $2S^0 + O_2 + H_2O \rightarrow S_2O_3^{2-} + 2H^+$ $S_2O_3^{2-} + 2O_2 + 2OH^- \rightarrow 2SO_4^{2-} + H_2O$	$hs\_ox=K_{\_hs\_ox}*H_2S*O_2$ $s0\_ox=K_{\_s0\_ox}*S^0*O_2$ $s23\_ox=K_{\_s23\_ox}*S_2O_3*O_2$
S^0 disproportionation $4S^0 + 3H_2O \rightarrow 2H_2S + S_2O_3^{2-} + 2H^+$	$Disprop=Kdisp*S^0$
Thiodenitrification $3H_2S + 4NO_3^- + 6OH^- \rightarrow 3SO_4^{2-} + 2N_2 + 6H_2O$	$hs\_NO3=K_T*H_2S*NO_3$ $hs\_NO2= K_T*H_2S*NO_2$
Mn oxidation and reduction $4Mn^{2+} + O_2 + 4H^+ \rightarrow 4Mn^{3+} + 2H_2O$ $4Mn^{3+} + O_2 + 6OH^- \rightarrow 4MnO_2 + 6H_2O$	$mn\_ox=K_{\_mn\_ox}*O_2*Mn(II)$ $mn\_ox2=K_{\_mn\_ox2}*O_2*Mn(III)$

$2MnO_2 + 7H^+ + HS^- \rightarrow 2Mn^{3+} + 4H_2O + S^0$ $2Mn^{3+} + HS^- \rightarrow 2Mn^{2+} + S^0 + H^+$	*mn_rd=K_mn_rd*Mn(IV)*H2S* *mn_rd2=K_mn_rd2*Mn(III)*H2S*
Fe oxidation and reduction $4Fe^{2+} + O_2 + 2H_2O \rightarrow 4Fe^{3+} + 4OH^-$ $2Fe_2^{+} + MnO_2 + 2H_2O \rightarrow 2FeOOH + Mn^{2+} + 2H^+$ $10Fe^{2+} + 2NO_3^- + 12H^+ = 10Fe^{3+} + N_2 + 6H_2O$ $2FeOOH + H_2S \rightarrow 2Fe^{2+} + S^0 + 4OH^-$	*fe_ox=K_fe_ox*Fe(II)*O2* *fe_mnox=K_fe_mnox*Fe(II)*Mn(IV)* *fe_nox=K_fe_nox*Fe(II)*NO3* *fe_rd=K_fe_rd*Fe(III)*H2S*
P sorption/desorption and complexation	*Coprecip = (fe_rd - fe_ox- fe_mnox)/2.7 -(mn_ox - mn_ox2 + mn_rd - mn_rd2)/0.66*
Phy growth rate	$GrowthPhy = K_{NF}\ f_t(T)\ f_i(i)\ min\{\ f_P(PO_4), f_N(NO_3 NO_2, NH_4$ $f_t(T) = 0.2 + 0.22(\exp(0.21T) - 1)/(1 + 0.28\exp(0.21T))$ $f_P(PO_4) = \frac{PO_4}{K_{PO4} + PO_4}$ $f_N(NO_3, NO_2, NH_4) = f'_N(NO_3, NO_2) + f''_N(NH_4) = \frac{(NO_3 + NO_2)\exp(-K_{psi} NH_4)}{K_{NO_3} + (NO_3 + NO_2)} + \frac{NH_4}{K_{NH_4} + NH_4}$
Phy excretion rate	*ExcrPhy=KFD*Phy*
Phy mortality rate	*MortPhy=KFP*Phy*
Grazing of *Zoo*	*Grazing=GrazPhy+GrazPOP+GrazBact*
Grazing of *Zoo* on *Phy*	*GrazPhy=KFZ*Zoo*(Phy/Zoo)/(Phy/Zoo+KF)*
Grazing of *Zoo* on detritus	*GrazPOP=KPZ*Zoo*(POP/Zoo)/(POP/Zoo+KPP/0.001)*
Grazing of *Zoo* on bacteria	*GrazBact=* $Graz_{Bhe} + Graz_{Bae} + Graz_{Bhat} + Graz_{Baa} + Graz_{Bhe}$ $Graz_{Bhe}$ *=KBhaZ*Zoo*(Bhe/Zoo)/(Bhe/Zoo+ KBhe)*

	$Graz_{Bae} = K_{BaeZ} * Zoo * (Bae/Zoo)/(Bae/Zoo + K_{Bae})$ $Graz_{Bhat} = K_{BhaZ} * Zoo * (Bha/Zoo)/(Bha/Zoo + K_{Bha})$ $Graz_{Baa} = K_{BaaZ} * Zoo * (Baa/Zoo)/(Baa/Zoo + K_{Baa})$
Mortality of *Zoo*	$MortZoo = K_{ZP} * Zoo * Zoo$
Growth rate of *Bhe*	$C_{Bhe} = K_{Bhe}^{\max} \cdot (DcPM\_O_2 + DcDM\_O_2) \cdot f_{Bhe}(DON + PON) \cdot Bhe$ $f_{Bhe}(DON + PON) = \frac{PON + DON}{PON + DON + K_{Bhe}^{N}}$
Rate of mortality of *Bhe*	$Mort_{Bhe} = K_{Bhe}^{Mort} * Bhe^2$
Growth rate of *Bae*	$C_{Bae} = K_{Bae}^{\max} \cdot (Nitrif1 + Nitrif2 + S^0\_ox + S_2O_3\_ox + mn\_($ $+ fe\_ox) f_{Bae}^{NP}(NH_4, PO_4) \cdot Bae$ $f_{Bae}^{NP}(NH_4, PO_4) = \min\left\{\frac{NH_4}{NH_4 + K_{Bae}^{N}}, \frac{PO_4}{PO_4 + K_{Bae}^{P}}\right\}$
Rate of mortality of *Bae*	$Mort_{Bae} = K_{Bae}^{Mort} Bae^2$
Growth rate of *Bha*	$C_{Bha} = K_{Bha}^{\max}(DcPM\_NO_3 + DcDM\_NO_3 + DcPM\_SO_4 +$ $+ DcDM\_SO_4) f_{Bha}(DON + PON) Bha$ $f_{Bha}(DON + PON) = \frac{PON + DON}{PON + DON + K_{Bha}^{N}}$
Rate of mortality of *Bha*	$Mort_{Bhe} = K_{Bhe}^{Mort} Bha^2$
Growth rate of *Baa*	$C_{Baa} = K_{Baa}^{\max}(mn\_rd + fe\_rd + hs\_ox + hs\_NO3 + hs\_NO2 +$ $+ anammox) f_{Baa}^{NP}(NH_4, PO_4) Baa$ $f_{Baa}^{NP}(NH_4, PO_4) = \min\left\{\frac{NH_4}{NH_4 + K_{Baa}^{N}}, \frac{PO_4}{PO_4 + K_{Baa}^{P}}\right\}$
Rate of mortality of *Baa*	$Mort_{Baa} = K_{Baa}^{Mort} Baa^2$

A detailed description of the biogeochemical model is given in Yakushev (2013)-

This version of model considered the water column (from 0 to 90 m), BBL (from 90 to 91 m) and the sediments (from 91 to 91.5 m) (Fig. 3-2).

The transport of the model parameters was described according to equation (1). The vertical transport coefficient K_z was assumed to be constant in the BBL and the sediments, and was calculated as a function of density in the water column. For the water column the model was forced by the seasonal variability of vertical distributions of temperature and salinity in the vicinity of the Sleipner area (NODC data). The coefficient of the vertical turbulent exchange in the water column was calculated on the base of the Gargett (1984) formula.

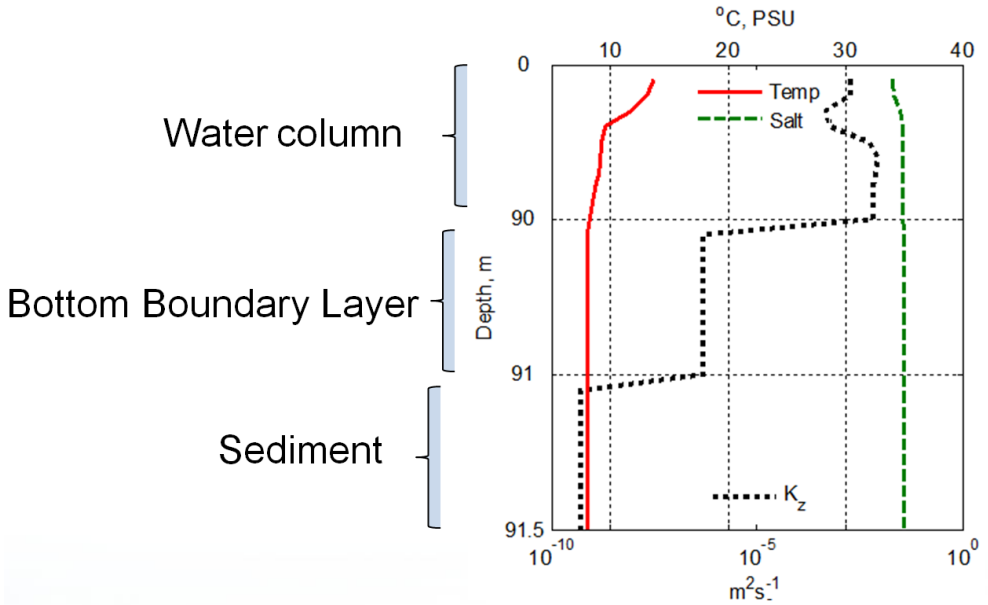

Fig. 3-2. Model domain and characteristic values of temperature, salinity and vertical transport coefficient.

RESULTS

Model is applied to simulate parameters distributions and fluxes changes connected with the variations of redox conditions at the sediment/water interface using the forcing data for the North Sea (Fig. 3-3,3-4,3-5,3-6).

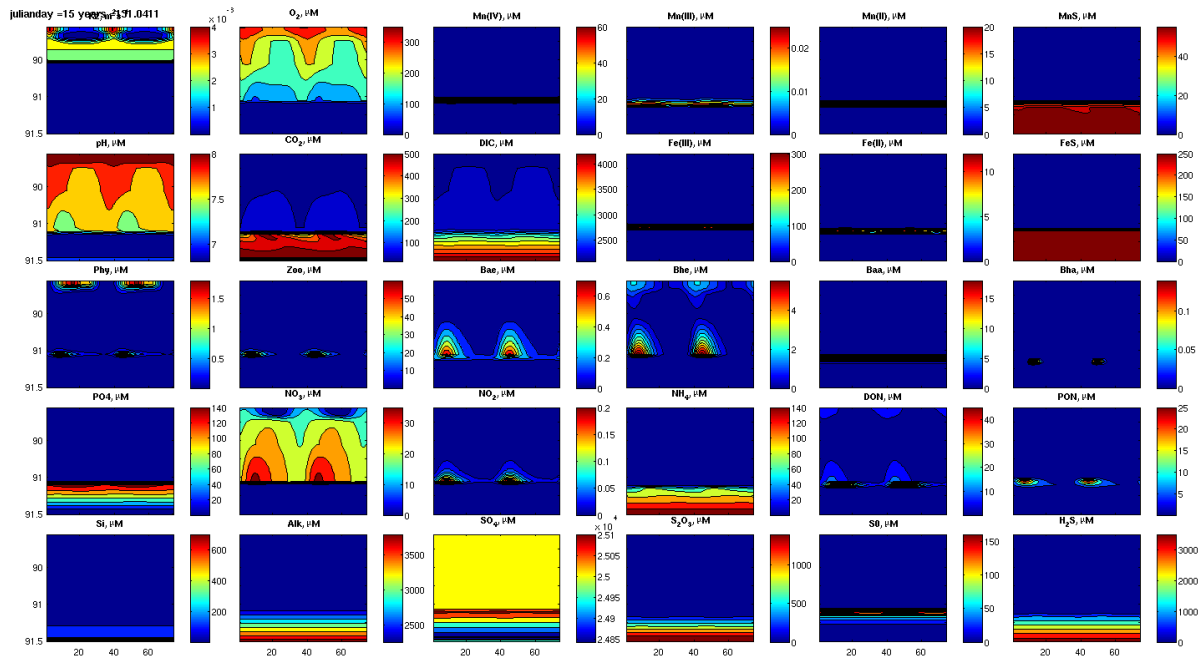

Fig. 3-3. Seasanal variability of the model parameters during 2 years simulations

The simulated distributions show that formation of the seasonal pycnocline (Fig. 3-3) restricts vertical transport of dissolved oxygen from the surface layer, meanwhile, its consumption in the bottom layer increases due to mineralization of OM produced in summer. This lead to changes of the oxygen concentrations in the BBL and at the sediment water interface (from about 180 uM in winter to 100 uM in summer (Fig. 3-4 and 3-5) and corresponding changes in CO_2 and pH.

The model simulated basic features of the seasonality ecosystem functioning, i.e. growth of concentrations of phototrophic organisms in summer, production of excessive OM and summer development of heteroreophic organisms and heteroprophic bacteria.

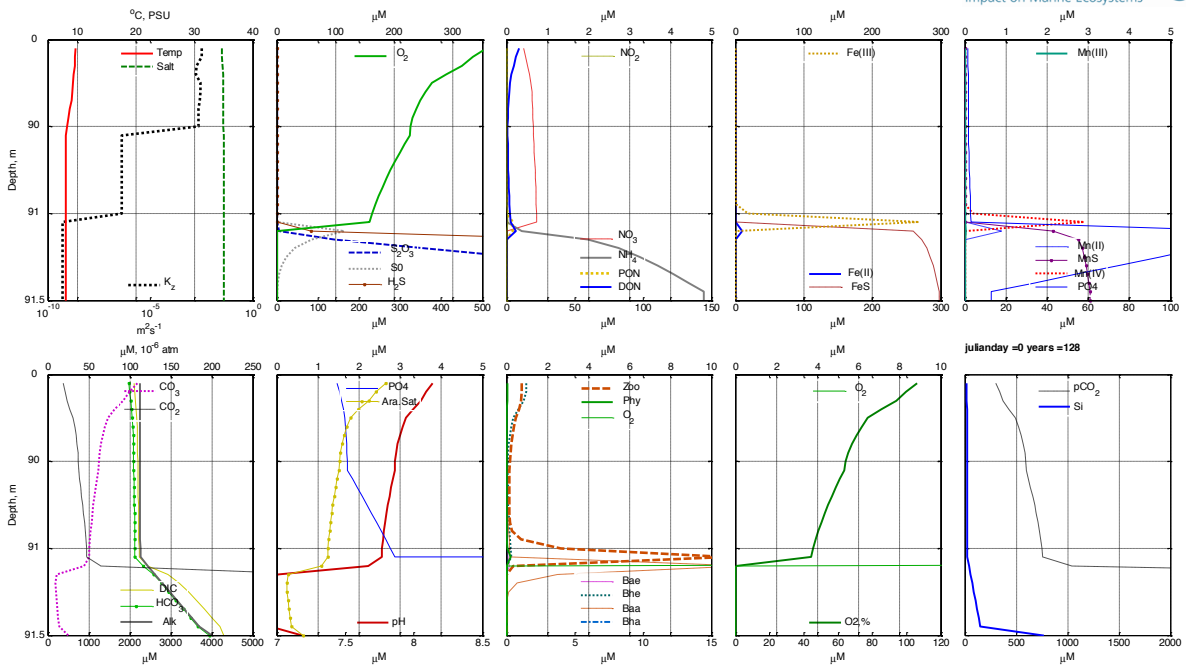

Fig. 3-4. Vertical distributions of the model parameters during the winter mixing

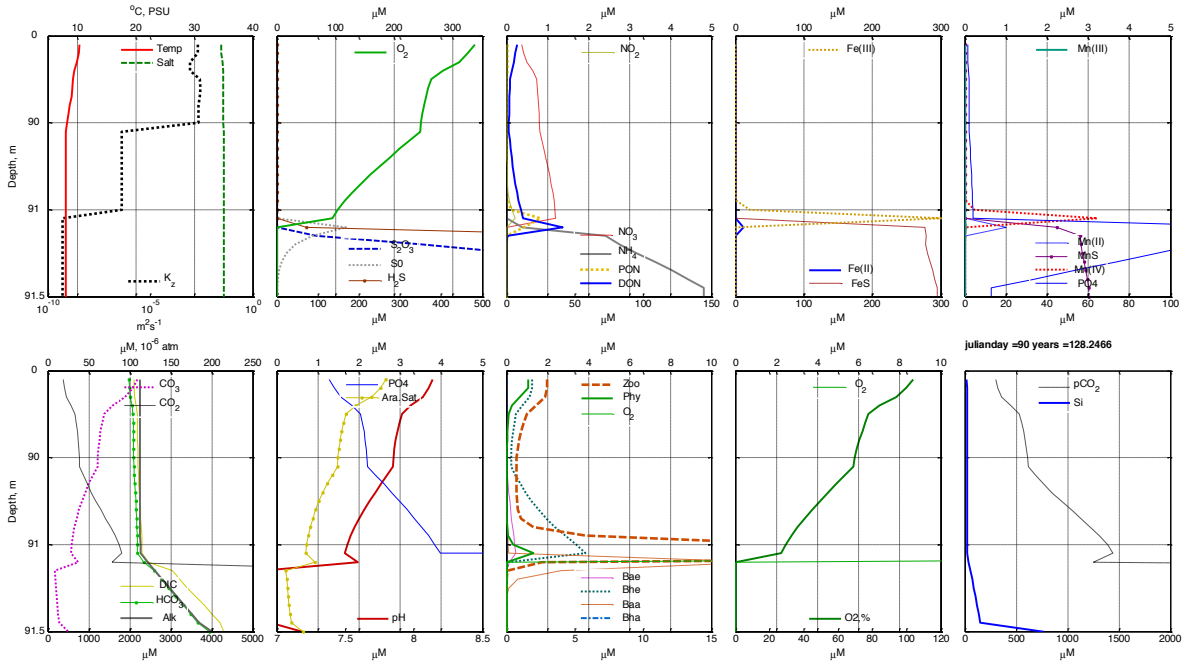

Fig.3-5. Vertical distributions of the model parameters during summer stagnation

Parameterization of autotrophic bacteria allowed to better simulate the fate of OM in changeable redox conditions, as it was shown for the water column (Yakushev et al., 2007)

The simulated oxygen concentrations ranges correspond to the observed ones (NODC data) and are well above the hypoxic threshold value. Nevertheless, these seasonal changes affect the nutrient and carbonate system concentrations and fluxes at the sediment-water boundary.

Our calculations showed, that pH decreased in summer compared to winter from 7.8 to 7.5 (pH Total scale) while aragonite saturation decreased from 1.3 to 0.8 (Fig.3-6).

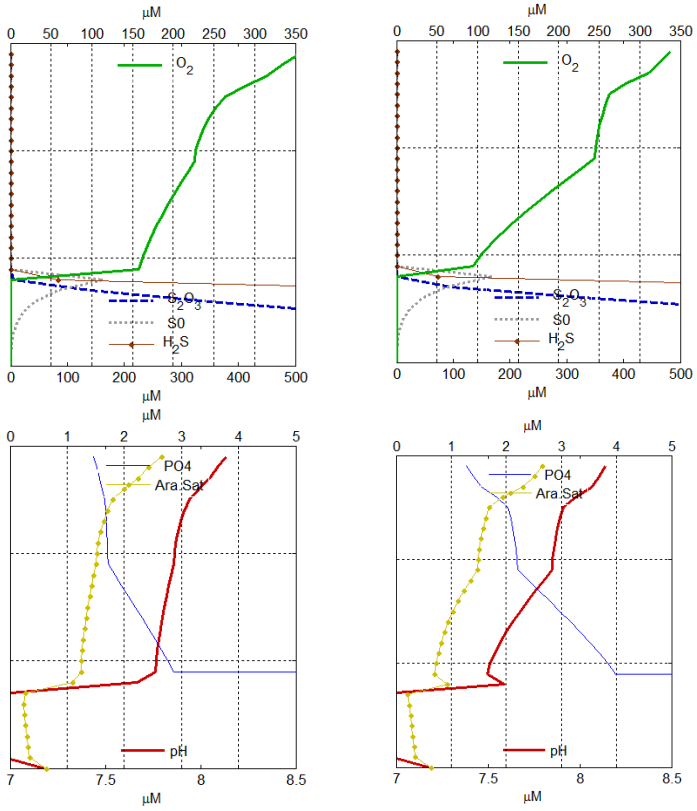

Figure 3-6. Simulated in the model seasonal distributions of dissolved oxygen, reduced sulfur forms (upper line), pH, aragonite saturation and phosphate (bottom line) in winter (left column) and in summer (right column).

These change in oxygen concentrations affected the cycles of redox metals, Mn and Fe and therefore trapping of phosphorus in the sediment. The model predicts an increase of phosphate concentration to 3.8 uM in summer compared to 2.8 uM in winter (Fig.3-6). This can be also connected with mineralization of OM. Nitrate concentration changes from 35 uM in summer compared to 25 uM in winter. This nitrate is consumed by the sediments

where denitrification starts after oxygen reaches suboxic values. After the nitrate depletion in the sediments, the process of sulphate reduction leads to appearance of sulphide and intermediate reduced sulphur species, thiosulfate and elemental sulphur.

The calculated distributions reflect the typical features of the redox interfaces in the sediments and the water column.

Data on distributions and variability of chemical parameters and results of the bottom-water flux measurements (WP4) will be used for this model validation and numerical experiments scenarios.

SUMMARY

On the base of the model simulations it was shown that:

- Seasonality in production and destruction of OM together with seasonal mixing can lead to redox conditions variations in the bottom boundary layer.
- Bacteria play a significant role in the fate of OM due to chemosynthesis (autotrophs) and consumption of DOM (heterotrophs).
- Changes in the bottom boundary layer redox conditions:
    - affect distribution of nutrients (N and P), redox metals (Mn and Fe) and carbonate system parameters;
    - determine magnitudes and directions of fluxes.
- Model can be used for analyzing and interpreting of data on sediment-water exchange and estimating consequences of forcing (i.e. CCS leakages).

PUBLICATIONS

Dewar, M., et al. 2013. Simulation of the near field physiochemical impact of CO2 leakage into shallow water in the North Sea. Energy Procedia. http://dx.doi.org/10.1016/j.egypro.2013.06.230

Dewar, M., et al. 2013. Small-scale modelling of the physiochemical impacts of CO2 leaked from sub-seabed reservoirs or pipelines with in the North Sea and surrounding waters. Mar. Pollut. Bull. http://dx.doi.org/10.1016/j.marpolbul.2013.03.005

Hvidevold, H. K., G. Alendal, T. Johannessen, and T. Mannseth. 2012. "Assessing Model Parameter Uncertainties for Rising Velocity of CO_2 Droplets Through Experimental Design." *International Journal of Greenhouse Gas Control* 11 (November 1): 283–289. doi:10.1016/j.ijggc.2012.09.008.

Hvidevold, H. K., G. Alendal, T. Johannessen, and T. Mannseth. 2013. "Assessing Model Uncertainties Through Proper Experimental Design." *Energy Procedia* 37 : 3439–3446. doi:10.1016/j.egypro.2013.06.233.

REFERENCES

Avlesen, H., Berntsen, J. and Espelid, T.O. A convergence study of two ocean models applied to a density driven flow. International Journal for Numerical Methods in Fluids, (2001), 36:639-657.

Baird M.H.I. and J.F. Davidson. 1962. Gas absorption by large rising bubbles, Chemical Engineering Science, Volume 17, Issue 2, Pages 87-93, ISSN 0009-2509, 10.1016/0009-2509(62)80020-7.

Bigalke, N. K., Enstad, L. I., Rehder, G. and Alendal, G., 2010. Terminal velocities of pure and hydrate coated CO_2 droplets and CH4 bubbles rising in a simulated oceanic environment, Deep-Sea Research Part I-Oceanographic Research Papers, 57(9), 1102-1110

Bigalke, N. K., Rehder, G. and Gust, G., 2008. Experimental Investigation of the Rising Behavior of CO_2 Droplets in Seawater under Hydrate-Forming Conditions, Environmental Science & Technology, 42(14), 5241-5246.

Blackford, J. C., N. Jones, R. Proctor, and J. Holt (2008), Regional scale impacts of distinct CO2 additions in the North Sea, Mar. Pollut. Bull., 56, 1461-1468, doi:10.1016/j.marpolbul.2008.04.048.

Bergh, J. and Berntsen, J., The surface boundary condition in nonhydrostatic ocean models, Ocean Dynamics, 60, 2010, pp. 317–330.

Bergh,J. and Berntsen,J., Numerical studies of wind forced waves with a non-hydrostatic model, Ocean Dynamics, 59, 2009, pp. 1025–1041.

Berntsen, H., Z. Kowalik, S. Sælid, and K. Sørli. "Efficient numerical simulation of ocean dynamics by splitting procedure." Model. Ident. Control 2 (1981): 181-199.

Berntsen, J. and Einar Svendsen, Using the SKAGEX dataset for evaluation of ocean model skills, Journal of Marine Systems, Volume 18, Issue 4, January 1999, Pages 313-331, ISSN 0924-7963, http://dx.doi.org/10.1016/S0924-7963(97)00111-5.

Berntsen, J. Users guide for a modesplit sigma-coordinate numerical ocean model. Tech. rep.,, Department of Mathematics, Bergen: University of Bergen, 2000.

Berntsen, J., J. Xing, and G. Alendal. "Assessment of non-hydrostatic ocean models using laboratory scale problems." Cont. Shelf Res. 26 (2006): 1433–1447.

Berntsen,J. and Xing,J. and Alendal,G. Assessment of non-hydrostatic ocean models using laboratory scale problems. Continental Shelf Research, 26(2006), pp. 1433–1447.

Berntsen,J., Xing,J. and Davies,A.M. Numerical studies of internal waves at a sill: sensitivity to horizontal size and subgrid scale closure. Continental Shelf Research., 28(2008), pp.1376—1393.

Berntsen,J., Xing,J. and Davies,A.M. (2009), Numerical studies of flow over a sill: sensitivity of the non-hydrostatic e□ects to the grid size, Ocean Dynamics, 59, 2009, pp. 1043–1059.

Bozec, Y., H. Thomas, K. Elkalay, and H. J. W. de Baar., 2005. The continental shelf pump for CO2 in the North Sea-Evidence from summer observation, Mar. Chem., 93, 131-147, doi:10.1016/j.marchem.2004.07.006.

Bozzano, G. and Dente, M., 2001. Shape and terminal velocity of single bubble motion: a novel approach, Computers & Chemical Engineering, 25(4-6), 571-576.

Caldeira, K., and M. E. Wickett., 2005. Ocean model predictions of chemistry changes from carbon dioxide emissions to the atmosphere and ocean, J. Geophys. Res., 110, C09S04, doi:10.1029/2004JC002671.

Calderbank, P. H., D. S. L. Johnson, and J. Loudon, Mechanics and mass transfer of single bubbles in free rise through some Newtonian and non-Newtonian liquids, Chem. Eng. Sc., 25, 235-256, 1970.

Carr and Davies. The motion of an internal solitary wave of depression over a fixed bottom boundary in a shallow, two-layer fluid. Phys Fluids 18(1):016,601–1–016,601–10, 2006

Chen, B. Nishio M., Song Y. and Akai M., 2009. The fate of CO2 bubble leaked from seabed. Energy Procedia, Vol. 1. Issue: 1. pp. 4969-4976

Chen, B., Song Y., Nishio M. and Akai M., 2003. Large-eddy simulation of double cloud formation induced by CO2 dissolution in the ocean, Tellus Series B, 55: 723– 730.

Chen, B., Song Y., Nishio M, Someya S. and Akai M., 2005. Modelling near-field dispersion from direct injection of carbon dioxide into the ocean, J. Geophys. Res., 110, C09S15, doi:10.1029/2004JC002567.

Clift, R., Grace, J. R. and Weber, M. E., 1978. Bubbles, drops and particles, Academic P.

Davenport W.G., F.D. Richardson and A.V. Bradshaw. 1967. Spherical cap bubbles in low density liquids, Chemical Engineering Science, Volume 22, Issue 9, Pages 1221-1235, ISSN 0009-2509, 10.1016/0009-2509(67)80188-X.

Dewar, M., et al. 2013. Small-scale modelling of the physiochemical impacts of CO2 leaked from sub-seabed reservoirs or pipelines with in the North Sea and surrounding waters. Mar. Pollut. Bull. http://dx.doi.org/10.1016/j.marpolbul.2013.03.005

Duan. Z., Shide Mao, A thermodynamic model for calculating methane solubility, density and gas phase composition of methane-bearing aqueous fluids from 273 to 523 K and from 1 to 2000 bar, Geochimica et Cosmochimica Acta, Volume 70, Issue 13, 1 July 2006, Pages 3369-3386, ISSN 0016-7037, 10.1016/j.gca.2006.03.018.

Espinoza, D. N. and Santamarina, J. C., 2010. Water-CO2-mineral systems: Interfacial tension, contact angle, and diffusion—Implications to CO2 geological storage, Water Resour. Res., 46(7), W07537.

Guthrie R.I.L. and A.V. Bradshaw. 1973. Spherical capped gas bubbles rising in aqueous media, Chemical Engineering Science, Volume 28, Issue 1, Pages 191-203, ISSN 0009-2509, 10.1016/0009-2509(73)85100-0.

Haberman, W. L., and Morton, R. K., 1954. An experimental study of bubbles moving in liquid. Proc., ASCE, New York, 387.

He, Y., Stanev, E.V., Yakushev, E., Staneva, J. 2012. Black Sea biogeochemistry: response to decadal atmospheric variability during 1960-2000s inferred from numerical modeling, Marine Environmental Research, 77, 90-102.

IPCC, 2005. IPCC Special Report on Carbon Dioxide Capture and Storage. Prepared by Working Group III of the Intergovernmental Panel on Climate Change. 2005. Metz, B., Davidson, O., de Coninck, H.C., Loos, M., Meyer, L.A., (Eds.). Cambridge University Press. Cambridge, United Kingdom and New York. NY. USA. 442.

Ito. M, 1984. Chemical handbook, 3rd ed. Tokyo: The Chemical Society of Japan, Maruzen Publishing Company; 553–558.

Jähne, B., G. Heinz, and W. Dietrich., 1987, Measurement of the diffusion coefficients of sparingly soluble gases in water, J. Geophys. Res., 92(C10), 10767–10776, doi:10.1029/JC092iC10p1076 7

Johnson, A. I., Besik, F., and Hamielec, A. E., 1969. Mass transfer from a single rising bubble. Can. J. Chem. Engrg., 47, 559–564.

Kamyshny Jr., A., E.V. Yakushev, G. Jost, and O.I. Podymov. 2013. Role of Sulfide Oxidation Intermediates in the Redox Balance of the Oxic–Anoxic Interface of the Gotland Deep, Baltic Sea. In: E.V. Yakushev (ed.), Chemical Structure of Pelagic Redox Interfaces: Observation and Modeling, Hdb Env Chem (2013) 22: 95–120

Klusman, R.W., 2003. Rate measurements and detection of gas microseepage to the atmosphere from an enhanced oil recovery/sequestration project, Rangely, Colorado, USA. Applied Geochemistry 18, 1825–1838.

Kowalik, Z. and T. S. Murty. Numerical Modeling of Ocean Dynamics. Advanced Series on Ocean Engineering, V5 World Scientific, 1993.

Lewis E, Wallace DWR. 1998. Program Developed for CO_2 System Calculations. ORNL/CDIAC-105. Carbon Dioxide Information Analysis Center, Oak Ridge National Laboratory, U.S. Department of Energy, Oak Ridge, Tennessee. http://cdiac.ornl.gov/oceans/co2rprt.html

Lynch et.al,1995. Convergence Studies of Tidally-Rectified Circulation on Georges Bank. In: Quantitative Skill assessment for Coastal Ocean Models, Lynch,D.R. and Davies,A.M. (editors), American Geophysical Union.

Marshall, J., C. Hill, L. Perelman, and A. Adcroft. “Hydrostatic, quasi-hydrostatic and non- hydrostatic ocean modeling .” J. Geophysic. Res. 102 (1997): 5733–5752.

Marshall. W.L., E.U. Franck, Ion product of water substance 0-1000C 1-10000 bars new international formulation and its background, 1981. J. Phys. Chem. Ref. Data 10 (2) 295–304

Martinsen, E. A., and H. Engedahl. “Implementation and testing of a lateral boundary scheme as an open boundary condition for a barotropic model. .” Coast. Eng. 11 (1987): 603–637.

McGinnis, D.F. and Little, C. Predicting diffused-bubble oxygen transfer rate using the discrete-bubble model, 2002. Water Research 36, 4627-4635

McGinnis, D.F., J. Greinert, Y. Artemov, S.E. Beaubien, and A. Wüest.,2006. Fate of rising metahne bubbles in stratified waters: How much methane reaches the atmosphere? J. Geophys. Res., 111, C09007, doi:10.1029/2005JC003183
McGinnis, D. F., M. Schmidt, T. DelSontro, S. Themann, L. Rovelli, A. Reitz, and P. Linke., 2011. Discovery of a natural CO_2 seep in the German North Sea: Implications for shallow dissolved gas and seep detection, J. Geophys. Res., 116, C03013, doi:10.1029/2010JC006557

Mellor, G.L. and T. Yamada. Development of a turbulence closure model for geophysical fluid problems. Reviews of Geophysics and Space Physics, 20:851– 875, 1982.

Motarjemi, M., and G.J. Jameson, Mass transfer from very small bubbles - the optimal bubble size for aeration, Chem. Eng. ScL, 33, 1415-1423, 1978.

Ozaki, M., Minamiura, J., Kitajima, Y., Mizokami, S., Takeuchi, K. and Hatakenaka, K., 2001. CO2 ocean sequestration by moving ships, Journal of Marine Science and Technology, 6(2), 51-58.

Pakhomova, S.V., E.V. Yakushev, 2013. On the role of iron and manganese species in the formation of the redox-interface structure in the Black Sea, Baltic Sea and Oslo Fjord In: E.V. Yakushev (ed.), Chemical Structure of Pelagic Redox Interfaces: Observation and Modeling, Hdb Env Chem (2013) 22: 67–94

QICS, 2012. QICS: Quantifying and Monitoring Potential Ecosystem Impacts of Geological Carbon Storage. [online] Available at: < http://www.bgs.ac.uk/qics/home.html> [Accessed 20 March 2012].

Ranz W E & Marshall W R, Jr., 1952. Evaporation from drops. Parts I & II. Chem. Eng. Progr. 48:141-6; 173-80.

Rehder, G., P. W. Brewer, E. T. Peltzer, and G. Friederich., 2002, Enhanced lifetime of methane bubble streams within the deep ocean, Geophys. Res. Lett., 29(15), 1731, doi:10.1029/2001GL013966./2005JC003183.

Rygg, Kristin; Alendal, Guttorm; Haugan, Peter M.. Flow over a rounded backward-facing step, using a z-coordinate model and a sigma-coordinate model. Ocean Dynamics 2011 ;Volum 61.(10) s. 1681-1696 UiB UNI

Saruhashi. K, Tansan-gasu-to-tansan-busshitsu, 1970 in: S. Horibe (Ed.), Kaisui-no-kagaku, Tokai Univ. Press, Tokyo, pp. 3.3.2.242–3.3.2.268 (in Japanese).

Someya, S., Bando, S., Song, Y., Chen, B. and Nishio, M., 2005. DeLIF measurement of pH distribution around dissolving CO2 droplet in high pressure vessel, International Journal of Heat and Mass Transfer, 48(12), 2508-2515.

Song, Y., M. Nishio, B. Chen, S. Someya, T. Uchida, and M. Akai 2002. Measurement of the density of CO2 solution by Mach-Zehnder Interferometry, Ann. N. Y. Acad. Sci., 972, 206– 212.

Thomas, H., et al. 2007. Rapid decline of the CO2 buffering capacity in the North Sea and implications for the North Atlantic Ocean, Global Biogeochem. Cycles, 21, GB4001, doi:10.1029/2006GB002825

Thiem, Ø., Carr, M., Berntsen, J., and Davies, P.A Numerical simulation of internal solitary wave - induced reverse flow and associated vortices in a shallow, two-layer fluid benthic boundary layer. Ocean Dynamics, Vol. 61, No. 6, pages 857-872, 2011.
doi:10.1007/s10236-011-0396-5

Tishchenko. P., H. Christian, W. Klaus, S.W. Chi., 2005. Calculation of the stability and solubility of methane hydrate in seawater, Chemical Geology, Volume 219, Issues 1–4, Pages 37-52, ISSN 0009-2541, 10.1016/j.chemgeo.2005.02.008.

Unesco., 1981. Tenth Report of the Joint Panel on Oceanographic Tables and Standards. Unesco Technical Papers in Marine Science, No. 36, 24–29.

Van Heuven, S., D. Pierrot, J.W.B. Rae, E. Lewis, and D.W.R. Wallace. 2011. MATLAB Program Developed for CO2 System Calculations. ORNL/CDIAC-105b. Carbon Dioxide Information Analysis Center, Oak Ridge National Laboratory, U.S. Department of Energy, Oak Ridge, Tennessee. doi: 10.3334/CDIAC/otg.CO2SYS_MATLAB_v1.1

Xing,J., Davies,A.M. and Berntsen,J., Free surface, current profile and buoyancy e□ects upon internal wave energy flux profiles in sill regions, Mathematics and Computers in Simulation, 80, 2009, pp. 786–793.

Yakushev E.V., Pollehne F., Jost G., Umlauf L., Kuznetsov I., Schneider B. 2007. Analysis of the water column oxic/anoxic interface in the Black and Baltic seas with a Redox-Layer Model, Marine Chemistry, 107, 388-410

Yakushev E., Pakhomova S., Sørensen K., Jens S. 2009. Importance of the different manganese species in the formation of water column redox zones: Observations and modelling, Marine Chemistry, 117, 59–70.

Yakushev, E.V., I. S. Kuznetsov, O. I. Podymov, H. Burchard, T. Neumann, F. Pollehne. 2011. Modeling of influence of oxygenated inflows on biogeochemical structure of the Gotland Sea, central Baltic Sea: changes in distribution of manganese, Computers and Geosciences, 37, 398–409

Yakushev, E., 2013. RedOx Layer Model: A Tool for Analysis of the Water Column Oxic/Anoxic Interface Processes. In: E.V.Yakushev (ed.) Chemical Structure of Pelagic Redox Interfaces: Observation and Modeling, Hdb Env Chem (2013) 22, 203–234.

Yakushev, E., Sørensen, K. 2013. On seasonal changes of the carbonate system in the Barents Sea: observations and modelling, Marine Biology Research 9(9), 822-830

Yang, H. Q. and A.j. Przekwas. “A comparative study of advanced shock-capturing schemes applied to burger’s equation .” J. Comput. Phys. 102 (1992): 139–159.

Zheng, L. and Yapa, P. D., 2002. Modeling gas dissolution in deepwater oil/gas spills, Journal of Marine Systems, 31(4), 299-309

.